Modeling and simulation of diffusion

Jing-Rebecca Li

N° d'ordre:

MÉMOIRE

Présenté pour obtenir

L' HABILITATION À DIRIGER DES RECHERCHES

Spécialité: Mathématiques

par

Jing-Rebecca Li

Modelisation et simulation de la diffusion

Soutenue le 16 décembre 2013 devant la Commission d'examen:

M.	Francois Alouges	
Mme.	Luisa Ciobanu	
M.	Matthias Ehrhardt	(Rapporteur)
M.	Jean-Frederic Gerbeau	
M.	Patrick Joly	
M.	Frédéric Lagoutière	(Rapporteur)

Rapporteurs:

M.	Christophe Besse

Thèse préparée au
Département de Mathématiques d'Orsay
Laboratoire de Mathématiques (UMR 8628), Bât. 425
Université Paris-Sud 11
91 405 Orsay CEDEX

Résumé

Deux concepts très importants dans mes travaux sont ceux de la diffusion (mouvement aléatoire des particules) et de ceux de la transformée de Fourier. La diffusion des particules peut être décrite par l'équation de la diffusion, dont la solution fondamentale a un forme beaucoup plus complexe que sa transformée de Fourier.

Tout d'abord, nous profitons de la forme spéciale de la transformée de Fourier (dans l'espace) de la fonction de Green de l'équation de diffusion pour formuler des méthodes numériques qui sont locales en temps pour la solution des équations avec mémoire.

L'idée principale est que la solution sera calculée dans le domaine de Fourier, pour éviter d'évaluer les intégrales de convolution en temps portent la « mémoire ». Ce travail a été rendu possible par le développement d'une quadrature adaptée de l'intégrale de Fourier où un petit nombre de points dans la variable de Fourier était suffisant pour une bonne résolution du problème dans l'espace physique, sur un intervalle de temps important. En particulier, nous avons développé une méthode numérique pour simuler la diffusion dans des domaines non bornés avec sources et l'avons appliquée à la modélisation de la croissance des cristaux, à l'aide du modèle du champ de phase. Puis, afin d'étendre cette approche à des problèmes aux limites, nous avons abordé la question de l'évaluation des potentiels de simple couche et de double couche sur le bord du domaine. Enfin, nous avons généralisé l'idée de remplacer les intégrales de convolution en temps par une quadrature efficace dans le domaine de Fourier, aux intégrales et aux dérivés d'ordres fractionnaires, et obtenu une borne rigoureuse de l'erreur de quadrature. Nous avons aussi appliqué cette approche à une équation des ondes fractionnaire.

En 2010, j'ai commencé à appliquer les outils numériques et analytiques à l'équation de Bloch-Torrey, dans le domaine de l'imagerie par résonance magnétique de la diffusion (IRMd) du cerveau. Ce travail a commencé dans le cadre d'une collaboration avec des physiciens d'IRM de Neurospin. Nous avons essayé d'expliquer la relation entre la géométrie cellulaire, la perméabilité membranaire et le signal d'IRMd obtenu.

Certaines difficultés de la modélisation et de la simulation du signal d'IRMd au niveau de l'échelle de temps et de l'espace viennent de la physique et de la biologie d'IRMd du cerveau. Premièrement, pour des raisons biologiques et techniques, l'IRMd ne peut mesurer que des temps de diffusion compris entre une et cent millisecondes, correspondant à une distance de diffusion moyenne de 2,5 à 25 micromètres. Cette distance est moyennée sur toutes les molécules d'eau, et la distance de diffusion réelle peut être différente selon que la localisation, au début de la mesure, des molécules d'eau : dans les corps neuronaux, dans les neurites (dendrites et axones) ou dans l'espace extra-cellulaire. Deuxièmement, certaines caractéristiques de la matière grise du cerveau rendent l'analyse et la simulation très difficiles :

1. Les cellules sont géométriquement complexes. Les neurones ont un corps solide, mesurant 1 à 10 micromètres de diamètre auquel sont attachés de longues neurites (axones et dendrites) qui mesurent de l'ordre d'un micromètre de diamètre et de plusieurs centaines de micromètres de longueur.
2. Les cellules ont une répartition très dense. Les corps neuronaux occupent 12% du volume du cortex cérébral, les axones 34%, les dendrites 35%, l'espace extracellulaire 6%, pour une largeur moyenne de 10 à 30 nanomètres.
3. L'organisation cellulaire est complexe. Les cellules du cortex sont organisées en couches, avec des colonnes de cellules liant différentes couches.
4. Les cellules sont perméables. En général, l'eau peut se déplacer entre les cellules et l'espace extracellulaire.

La résolution d'IRMd est de l'ordre de 1 mm^3, ce qui signifie que chaque pixel de l'image affiche les caractéristiques de diffusion moyennées dans un volume de tissu (voxel) de 1 mm^3, ce qui est très grand devant les échelles spatiales cellulaires. Pour modéliser le signal de l'IMRd dans un voxel, il faut simuler l'aimantation à l'intérieur de ce voxel et calculer son intégrale au

moment de l'écho. La distance de diffusion moyenne ne dépassant pas 25 micromètres, il suffit de faire le calcul dans un domaine légèrement plus grand qu'un voxel pour tenir compte de la diffusion de toutes les molécules d'eau qui auront « vu » ce voxel durant le temps de diffusion.

De plus, si nous supposons que le voxel contient un environnement cellulaire qui ne varie pas beaucoup à dans le voxel, nous utilisons un domaine de calcul plus petit, celui-ci devra ne contenir qu'une « portion représentative » du tissu dans le voxel. Pour étudier le lien entre l'atténuation du signal d'IRMd et les propriétés géométriques du tissu, tels que le diamètre moyen des cellules et la fraction volumique cellulaire, nous avons généré, dans un premier temps, des domaines de calcul qui contiennent une configuration cellulaire à étudier. A terme, nous envisageons des simulations sur beaucoup de configurations pour obtenir des résultats statistiquement significatifs. Actuellement, nous construisons une seule configuration cellulaire et résolvons le problème forward et inverse associé.

Le signal d'imagerie par résonance magnétique de diffusion dans le tissu biologique peut être considéré comme une sorte de « transformée de Fourier » de la fonction de densité de probabilité de déplacement de l'eau dans les milieux hétérogènes. L'aimantation des protons de l'eau en tissu biologique en présence d'impulsions du gradient de champ magnétique, peut être modélisée par une équation aux dérivées partielles (EDP), l'équation de Bloch-Torrey microscopique à compartiments multiples. Cette EDP peut être comprise comme l'attribution aux molécules d'eau en milieu hétérogène, d'une fréquence spatiale qui dépend de leurs positions. Le signal d'IRMd est l'intégrale de la solution de cette EDP au moment de l'écho.

Nous avons résolu numériquement cette EDP en couplant une discrétisation spatiale cartésienne standard avec une discrétisation en temps adaptative (Runge-Kutta Chebyshev « RKC ») et nous avons étudié les caractéristiques de la diffusion d'un modèle de la matière grise du cerveau constitué de cellules cylindriques et sphériques dans l'espace extracellulaire. Puis, par homogénéisation, nous avons formulé un nouveau modèle macroscopique, sous forme d'un système d'équations aux dérivées ordinaires (EDO), pour le signal d'IRMd. Ensuite, nous avons montré par des simulations numériques que ce modèle d'EDO donne une bonne approximation du signal du modèle d'EDP complet pour des temps de diffusion relativement longs.

Je mentionne aussi le travail de deux doctorants que je co-encadre actuellement. Dang Van Nguyen (soutenu par le projet SIMUDMRI, ANR COSINUS 2010-2013) a couplé une discrétisation d'éléments finis avec la méthode RKC pour obtenir une discrétisation plus précise des surfaces cellulaires. Il travaille sur l'analyse du signal de l'IRMd des neurones isolés. Huan Tuan Nguyen (soutenu par une bourse de l'École Doctorale « Sciences et Technologies de l'Information, des Télécommunications et des Systèmes » ED STITS, 2010-2013) travaille sur le problème inverse du modèle d'EDO.

Enfin, j'envisage trois orientations futures de mes recherches dans l'IRMd.

1. En collaboration avec le centre Neurospin IRM, confronter les résultats numériques du modèle d'EDP avec les données expérimentales IRMd des ganglions (réseaux neuronaux) de l'Aplysie (limace de mer géante).
2. Prendre en compte l'écoulement sanguin dans les micro-vaisseaux du cerveau, via un nouveau modèle d'EDP.
3. Obtenir la formulation d'un nouveau modèle d'EDO valable aux temps de diffusion plus courts ou en présence des cellules plus grandes.

.

Mots-clefs : Diffusion, imagerie par resonance magnetic de la diffusion, équations avec memoire, l'équation integral.

Modeling and simulation of diffusion

Abstract

The first part of this thesis concerns the formulation of numerical methods that are local in time for the solution of equations with memory. The main idea is that the solution will be updated in the Fourier domain in order to avoid evaluating time convolution integrals that have memory. This work was made possible by the development of a good quadrature[31] of the Fourier integral where a small number of points in the Fourier variable were sufficient for a good resolution of the problem in the physical space over a large time interval.

First, we developed a numerical method to simulate diffusion in unbounded domains with sources and applied it to the modeling of crystal growth using the phase field model. Then, in order to extend this approach to boundary value problems, we addressed the issue of evaluating the single and double layer potentials on the boundary. Finally, we generalized the idea of replacing time convolution integrals by an efficient quadrature in the transform domain to fractional integrals and derivatives for general fractional orders and obtained a rigorous bound on the quadrature error. Then we applied this approach to a fractional wave equation.

The second part of the thesis concerns the specific application of diffusion magnetic resonance imaging (dMRI) in the brain. The effect on the MRI signal of the water proton magnetization in biological tissue in the presence of magnetic field gradient pulses can be modeled by a *microscopic* multiple compartment Bloch-Torrey partial differential equation (PDE). This PDE can be best understood as imparting a spatially dependent frequency to diffusing particles in a heterogeneous medium. The dMRI signal is the integral of the solution of this PDE at the echo time.

First, we numerically solved this PDE by coupling a standard Cartesian spatial discretization with an adaptive time discretization and studied the diffusion characteristics of a tissue model of the brain gray matter made up of cylindrical and spherical cells embedded in the extra-cellular space. Next we formulated a new *macroscopic* ODE model for the dMRI signal by mathematical homogenization. Then we showed by numerical simulations that this ODE model gives a good approximation of the dMRI signal of the full PDE model at relatively long but still physically realistic diffusion times relevant to dMRI in the brain.

Finally, I will describe some future research directions in dMRI. The first is the experimental validation of the PDE model by imaging the ganglia (neuronal network) of the Aplysia (giant sea slug), to be conducted at the MRI center Neurospin. The second is the inclusion of blood flow in the bran micro-vessels in a new PDE model. The third is the formulation of a different ODE model valid at shorter diffusion times or in the presence of larger cells.

Keywords : Diffusion, diffusion magnetic resonance imaging, integral equation, equations with memory.

Remerciements

I would like to thank my post-doc supervisor at the Courant Institute, Leslie Greengard, as well as Thomas Hagstrom and Brad Alpert for teaching me all about time stepping methods and quadrature and for being available for discussions as well as providing me with invaluable pieces of code.

I also wish to thank my colleagues in the POEMS and DEFI teams at INRIA, Patrick Joly, Eliane Becache, Houssem Haddar, for the crash course on waves, homogenization, and French culture.

For my recent work on diffusion MRI I owe a great deal to the kindness and welcome shown to me by Denis Le Bihan, Cyril Poupon, Luisa Ciobanu of Neurospin, as well as by Denis Grebenkov of the PMC at Ecole Polytechnique.

I also need to thank my family, especially my husband Boris, and my children Milo and Arcadia.

Table des matières

Première partie

Introduction

The two most important concepts in this thesis are that of diffusion (random motion of particles) and that of the Fourier transform. First, we take advantage of the special form of the Fourier transform (in space) of the Green's function of the diffusion equation to formulate efficient time stepping methods for equations with memory. Second, we model and simulate the diffusion magnetic resonance imaging signal in biological tissue, which can be thought of as a kind of "Fourier transform" of the probability density function of water displacement in heterogeneous media.

The diffusion of a dilute solute in a solvent or the conduction of heat can be described by :

$$\mathbf{J} = -D\nabla u(\mathbf{r}, t),$$

where $u(\mathbf{r}, t)$ describes the concentration of the solute or the temperature at position $\mathbf{r}$ and time t, $\mathbf{J}$ is the rate of transfer per unit area, and D is a proportionality constant called the intrinsic diffusion coefficient that has the unit of $(length)^2/time$. Over each unit volume, we obtain the diffusion (or heat) equation :

$$\frac{\partial u}{\partial t} = \nabla D \nabla u(\mathbf{r}, t).$$

The fundamental solution for the diffusion equation in $\mathbb{R}^d$ is :

$$G\left(\mathbf{r}, Dt\right) := \frac{e^{-\|\mathbf{r}\|^2/4Dt}}{(4\pi Dt)^{\frac{d}{2}}}, \quad t > 0. \tag{1}$$

Even though G is a complicated function in $\mathbf{r}$ and t, its Fourier transform is rather simple :

$$\hat{G}(\mathbf{s}, Dt) := \int_{\mathbb{R}^d} e^{i\mathbf{s}\cdot\mathbf{x}} G(\mathbf{x}, Dt)\, d\mathbf{x} = e^{-\|s\|^2 Dt}. \tag{2}$$

To get back G from $\hat{G}$, we perform the inverse Fourier transform :

$$G(\mathbf{x}, Dt) = \frac{1}{(2\pi)^d} \int_{\mathbb{R}^d} e^{-i\mathbf{s}\cdot\mathbf{x}} \hat{G}(\mathbf{s}, Dt)\, d\mathbf{s}. \tag{3}$$

The first part of this thesis concerns the formulation of an efficient time-stepping method for the solution of the diffusion equation by moving into the Fourier domain at each time step, to take advantage of the fact that the expression in (2) gives rise to numerical methods that are local in time whereas the expression in (1) gives rise to time convolution integrals that have memory. This work was made possible by the development [31] of a good quadrature of the Fourier integral in (3) where a small number of points in the Fourier variable $\mathbf{s}$ are sufficient for a good resolution of the problem in the physical space over a large time interval.

First, we developed a numerical method to simulate diffusion in unbounded domains with sources. Then we applied it to the modeling of crystal growth using the phase field model. Next, in order to extend this approach to boundary value problems, we addressed the issue of evaluating single and double layer potentials on the boundary. Finally, we generalized the idea of replacing time convolution integrals by an efficient quadrature in the transform domain to fractional integrals and derivatives for general fractional orders

and obtained a rigorous bound on the quadrature error. Then we applied this approach to a fractional wave equation.

The second part of the thesis concerns the specific application of diffusion magnetic resonance imaging (dMRI) in the brain. This work comes out a collaboration I started in 2010 with the researchers of the high field MRI facility Neurospin.

The principle of (water proton) magnetic resonance imaging (MRI) is the following. Suppose r_1, r_2, r_3 are the axes of a 3D coordinate system. Inside the MRI scanner, there is a strong static magnetic field of magnitude B_0 applied along the positive r_3-direction, and the spins of the water protons inside the body become aligned to this magnetic field, resulting in a net magnetization in the positive r_3-direction. When a time-varying magnetic field (much weaker than the static magnetic field) is applied for a short time at the resonance frequency, $\omega_0 = \gamma B_0$, where $\gamma = 42.576$ MHz/Tesla is the gyromagnetic ratio, the net magnetization is tipped off the r_3-axis. For simplicity, we assume the net magnetization is tipped onto the $r_1 - r_2$ plane, then the oscillating magnetic field will be called a 90 degree pulse. The spins then precess around the r_3-axis, inducing a voltage in a receive coil. The net magnetization in the $r_1 - r_2$ (transverse plane to the direction of the main magnetic field) can be measured as a signal.

The net magnetization will realign along the r_3-direction, due to two relaxation effects : the spin-lattice relaxation of the net magnetization along the r_3-direction to its original value, and the spin-spin relaxation of the decay of the net magnetization in the $r_1 - r_2$ plane to zero. The rate constant of the first relaxation is called T_1 and the rate constant of the second kind of relaxation is called T_2. Both T_1 and T_2 vary according to the tissue environment. Additionally, the spin density also varies with the tissue environment.

Usually, in addition to T_2 (spin-spin) relaxation, local inhomogeneities also contribute to the signal decay. The latter can be cancelled by a refocusing 180 degree pulse, applied at $t = TE/2$ after the 90 degree pulse, producing an echo at TE, that gives a measured signal that will have the correct contribution from T_2. Such a sequence of applied magnetic fields is called a spin echo sequence.

The spatial encoding of the signal is obtained by applying additional magnetic fields in the r_3 direction, called magnetic field gradients, that vary linearly in space : $\mathbf{r} \cdot \mathbf{G_{im}}(t)$, where $\mathbf{G_{im}}(t)$ will be called the imaging gradient. In the rotating frame at the frequency ω_0, the complex transverse magnetization on the $r_1 - r_2$ plane, $M(\mathbf{r}, t) := M_{r_1}(\mathbf{r}, t) + IM_{r_2}(\mathbf{r}, t)$, I is the imaginary unit, obeys the Bloch Equation [8] :

$$\frac{\partial M(\mathbf{r}, t)}{\partial t} = -I\gamma \, \mathbf{r} \cdot \mathbf{G_{im}}(t) M(\mathbf{r}, t) - \frac{M(\mathbf{r}, t)}{T_2(\mathbf{r})}, \tag{4}$$

where $T_2(\mathbf{r})$ is the local spin-spin relaxation rate. The solution of Eq. 4 is

$$M(\mathbf{r}, t) = \rho(\mathbf{r}) \, e^{-t/T_2(\mathbf{r})} \, e^{-I\mathbf{r} \cdot \left(\gamma \int_0^t \mathbf{G_{im}}(s) \, ds\right)},$$

where $t = 0$ is the start of the 90 degree pulse and $\rho(\mathbf{r})$ is the spin density.

Even though 3D imaging is possible, most often the MRI signal is acquired in 2D, slice by slice. Suppose $r_3 \in [\left(l - \frac{1}{2}\right) \Delta r_3, \left(l + \frac{1}{2}\right) \Delta r_3]$ are the limits of the slice of interest. By choosing $\mathbf{G_{im}}(t) = (0, G_2, 0)$ for a time interval Δt_2 and then choosing $\mathbf{G_{im}}(t) =$

$(G_1, 0, 0)$ for a time interval Δt_1, then the magnetization at $\mathbf{r}$ at TE is

$$M(\mathbf{r}, t) = \rho(\mathbf{r})\, e^{-TE/T_2(\mathbf{r})}\, e^{-I(k_1 r_1, + k_2 r_2)},$$

where $k_1 = \gamma G_1 \Delta t_1$ and $k_2 = \gamma G_2 \Delta t_2$. The MRI signal, acquired at echo time $t = TE$, is the integral of the magnetization in that slice :

$$\hat{\mu}_l\,(k_1, k_2) = \int_{r_1, r_2} \mu_l(r_1, r_2)\, e^{-I(k_1 r_1 + k_2 r_2)} dr_1 dr_2, \tag{5}$$

where the contrast function is :

$$\mu_l(r_1, r_2) = \left(\int_{(l-\frac{1}{2})\Delta r_3}^{(l+\frac{1}{2})\Delta r_3} \rho(r_1, r_2, r_3)\, e^{-\frac{TE}{T_2(r_1, r_2, r_3)}}\, dr_3 \right). \tag{6}$$

It is clear that the MRI signal in Eq. 5 is the 2D Fourier transform of the contrast function in Eq. 6.

By the appropriate choice of G_1, G_2, and Δt_1 and Δt_2 the Fourier transform can be obtained at a set of 2D Fourier points. Then the inverse Fourier transform can be performed and then sampled at physical space points to obtain in each voxel, $V_{i,j,l}$ where

$$\begin{aligned} V_{i,j,l} := & \left[\left(i - \frac{1}{2} \right) \Delta r_1, \left(i + \frac{1}{2} \right) \Delta r_1 \right] \times \left[\left(j - \frac{1}{2} \right) \Delta r_2, \left(j + \frac{1}{2} \right) \Delta r_2 \right] \\ & \times \left[\left(l - \frac{1}{2} \right) \Delta r_3, \left(l + \frac{1}{2} \right) \Delta r_3 \right], \end{aligned}$$

an average value of the contrast function :

$$\bar{\mu}_l(i, j) \approx \int_{V_{i,j,l}} \rho(r_1, r_2, r_3)\, e^{-\frac{TE}{T_2(r_1, r_2, r_3)}}\, dr_1\, dr_2\, dr_3, \tag{7}$$

that can be displayed in an image. In (7) we can see two widely used contrast mechanisms in MRI, the spin density and the T_2 relaxation.

Besides the spin density and the T_2 relaxation, the water diffusion characteristics in the tissue can be another source of contrast. How this contrast is encoded is by the application of more magnetic field gradients. This gradient will be denoted the diffusion-encoding gradient $\mathbf{G_{df}}(t)$. One pulse of the gradient is applied in the direction $\mathbf{g}$ before 180 degree refocusing pulse and the same pulse after. The lack of complete refocussing is due to water diffusion and gives the diffusion MRI contrast.

The mathematical description of the complex transverse magnetization including effects of diffusion is called the Bloch-Torrey equation [106] :

$$\frac{\partial M(\mathbf{r}, t)}{\partial t} = -I\gamma\, \mathbf{r} \cdot \mathbf{G_{im}}(t)\, M(\mathbf{r}, t) - \frac{M(\mathbf{r}, t)}{T_2(\mathbf{r})} - I\gamma\, \mathbf{r} \cdot \mathbf{g} f(t)\, M(\mathbf{r}, t) + \nabla \cdot \Big(D(\mathbf{r}) \nabla M(\mathbf{r}, t) \Big), \tag{8}$$

where $\mathbf{G_{df}}(t) = \mathbf{g}\ f(t)$, $f(t)$ containing the time profile information of the diffusion-encoding gradient. The last term in the above equation concerns the diffusion (random movement) of water molecules.

The magnetic field gradients are usually applied in "pulses". The term "pulse" means that the magnetic field gradient is turned on only for a certain duration in time. The

usual notation is that the duration of the pulses is δ and the distance between the start of adjacent pulses is Δ. For example, for the standard Pulsed-Gradient Spin Echo (PGSE) [97] sequence, made of two rectangular pulses (duration δ, separated by a time interval $\Delta - \delta$, see Figure (1)) the profile $f(t)$ is :

$$f(t) = \begin{cases} 1, & t_1 \leq t \leq t_1 + \delta, \\ -1, & t_1 + \Delta < t \leq t_1 + \Delta + \delta, \\ 0, & \text{elsewhere}, \end{cases} \tag{9}$$

where t_1 is the starting time of the first pulse and $\frac{TE}{2}$, the time of the application of the 180 degree refocussing pulse, is between $t_1 + \delta$ and $t_1 + \Delta$.

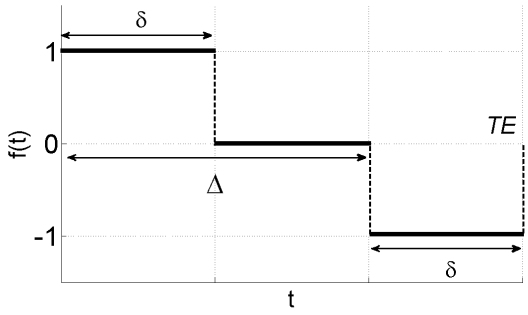

FIG. 1 – A PGSE sequence for $t_1 = 0$.

Under the assumption that water molecules experience a homogeneous (or homogenized) isotropic diffusion environment characterized by the diffusion coefficient D^{hom} inside the voxel $V_{i,j,l}$, the water molecules at position $\mathbf{r}_0 \in V_{i,j,l}$ at $t = t_1$ diffuse according to the probability density function :

$$u(\mathbf{r}, t) = \frac{e^{-\|\mathbf{r}-\mathbf{r}_0\|^2/4D^{hom}(t-t_1)}}{(4\pi D^{hom}(t-t_1))^{\frac{d}{2}}}, \quad d = 3,$$

where the support of $u(\mathbf{r}, t)$ is much smaller than $V_{i,j,l}$ because the diffusion distance in a dMRI experiment is much smaller than the size of a voxel (we have neglected those $\mathbf{r}_0$ that are close to the boundary of $V_{i,j,l}$).

Furthermore, under the assumption that $\delta \ll \Delta$ (the narrow pulse assumption), the influence of the diffusion-encoding magnetic field gradient pulse on the complex transverse magnetization due to water molecules starting at $\mathbf{r}_0$ at $t = t_1$ can be described by a gain of the complex phase $e^{-I\gamma \mathbf{g}\cdot\mathbf{r}_0\,\delta}$ between t_1 and $t_1 + \delta$. Then, the magnetization due to water molecules at position $\mathbf{r}$ at $t_1 + \Delta$ gain a complex phase $e^{I\gamma \mathbf{g}\cdot\mathbf{r}\,\delta}$ between $t_1 + \Delta$ and $t_1 + \Delta + \delta$. Thus, the effect on the MRI signal, compared to having no diffusion gradient $\mathbf{g}$, due to water molecules at $\mathbf{r}_0$ when $t = t_1$, is an *attenuation* (loss) of the signal :

$$\int_{\mathbf{r}\in V_{i,j,l}} \frac{e^{-\|\mathbf{r}-\mathbf{r}_0\|^2/4D^{hom}\Delta}}{(4\pi D^{hom}\Delta)^{\frac{d}{2}}}\, e^{I\gamma \mathbf{g}\cdot(\mathbf{r}-\mathbf{r}_0)\,\delta} = e^{-\gamma^2\delta^2\|\mathbf{g}\|^2 D^{hom}\Delta},$$

where we used the formula for the Fourier transform of the Green's function of the heat or diffusion equation.

If δ is not small compared to Δ, then in fact, the signal attenuation in the voxel $V_{i,j,l}$ is [106] :

$$S(b, TE) = e^{-D^{hom}\, b},$$

where the b-value is a weighting factor as defined in [59] and it is

$$b(\mathbf{g}, \delta, \Delta) = \gamma^2 \|\mathbf{g}\|^2 \delta^2 \left(\Delta - \delta/3\right), \tag{10}$$

for the PGSE sequence. The replacement of Δ by $\Delta - \delta/3$ accounts for pulses that are not narrow.

Including the effect of the diffusion-encoding gradient means that the image contrast function in (6) becomes :

$$\mu_l(r_1, r_2) = \left(\int_{(l-\frac{1}{2})\Delta r_3}^{(l+\frac{1}{2})\Delta r_3} c\, \rho(r_1, r_2, r_3)\, e^{-t/T_2(r_1,r_2,r_3)} e^{-D^{hom}(r_1,r_2,r_3)\, b}\, dr_3 \right). \tag{11}$$

The basis of diffusion weighted imaging is that the MRI signal is acquired with a diffusion gradient $\mathbf{g}$ as well as with no diffusion gradient. The first image (after inverse Fourier transform) is divided by the second image and the log of the ratio is divided by b get an estimate of $D^{hom}(r_1, r_2, r_3)$ in each voxel. This estimated value is called the "Apparent Diffusion Coefficient" (ADC), and serves as the contrast mechanism.

However, it was realized that when $\mathbf{g}$ is varied in magnitude or direction, the *ADC* changes significantly. Similarly, different values of the ADC are obtained when Δ is varied. In fact, by fixing the direction of $\mathbf{g}$ and Δ (as well as the pulse duration δ) and varying the amplitude $\|\mathbf{g}\|$, one can see clearly that the diffusion-induced MRI signal attenuation is not a decaying exponential in b. The reason for this is that in biological tissue, the diffusion environment seen by water molecules during the time period of Δ (tens of milliseconds) is not homogeneous due to the presence of cells membranes and other heterogeneities. It also cannot be described simply by a *homogenized* diffusion coefficient (or tensor) because Δ is not long enough.

The research that I will describe in the second part of this thesis is about explaining the relationship between the cellular geometry, cell membrane permeability, and the obtained dMRI signal attenuation. In other words, I would like to obtain a more accurate description of the image contrast function than (11). For simplicity, I will not, at this time, consider the effect of T_2 relaxation. And since I just want to understand the image contrast function in the physical domain, I will also neglect the imaging gradients.

Now I will describe some aspects of the physics and the biology of dMRI of the brain. DMRI is limited to a range of diffusion times it can measure due to biological and technical reasons. In the brain, diffusion times in the range of 1ms-100ms can be measured, associated to average diffusion distances of $2.5\mu m$-$25\mu m$. This distance is averaged over all water molecules, and the actual diffusion distance can be different depending on whether the water molecules started in the neuronal bodies, the neurites (dendrites and axons) or the extra-cellular space. There are some features of the brain gray matter that make analysis and simulation of diffusion in the brain gray matter very difficult :

1. Individual cells are geometrically complex. Neurons have a solid cell body, measuring 1 to 10 μm in diameter. Attached to the neuronal body are long protrusions

called neurites (axons and branching dendrites) that measure, respectively, 0.5 and 0.9 μm in average diameter, and can be several hundreds of μm in length. See Figure 2(a).

2. The cells are densely packed. Neuronal bodies occupy 12% of the brain cortex volume, axons, 34%, dendrites, 35%, and the extracellular space, 6% in volume and 10-30 nm in width. See Figure 2(b)
3. The cellular organization is complex. The cells of the cortex are organized into layers, with columns of cells linking the different layers.
4. The cells are permeable. Water can move between the cells and the extra-cellular space, except across the myelin layer of the myelinated axons.

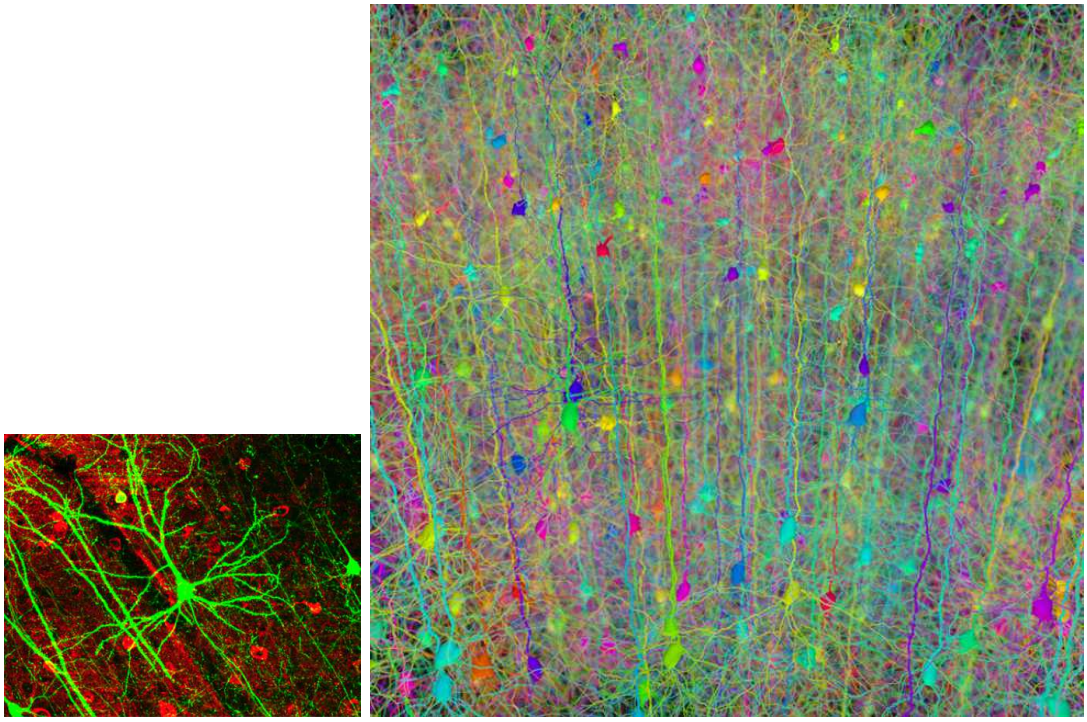

(a) GFP expressing pyramidal cell in mouse cortex.

(b) Forest of synthetic pyramidal dendrites grown using Cajal's laws of neuronal branching

FIG. 2 – Left : a single neuron has a complex shape, with a solid body and many long thin branching protrusions. Right : neurons are densely packed. *Source : Wikipedia Commons. (left) Dynamic Remodeling of Dendritic Arbors in GABAergic Interneurons of Adult Visual Cortex Wei-Chung Allen Lee, Hayden Huang, Guoping Feng, Joshua R. Sanes, Emery N. Brown, Peter T. So, Elly Nedivi PLoS Biology Vol. 4, No. 2, e29 DOI : 10.1371/journal.pbio.0040029. (right) PLoS Computational Biology Issue Image, Vol. 6(8) August 2010. PLoS Comput Biol 6(8) : ev06.i08. doi :10.1371/image.pcbi.v06.i08*

The resolution of dMRI is order of 1 mm^3, meaning each pixel in the image displays the averaged diffusion characteristics of a tissue volume (voxel) of 1 mm^3. This is very large compared to cell features, which vary from sub-micron (diameter of neurites) to tens of microns (neuronal bodies and glial cells) in the brain.

To simulate the dMRI signal attenuation in a voxel V, one would have to simulate the magnetization inside V and compute its integral at echo time. At physically realistic

dMRI diffusion times of tens of milliseconds, the average diffusion distance is no more than 25 microns. Thus, it would suffice to simulate in a computational domain that that is slightly larger than a voxel to account for the diffusion of all water molecules that will "see" this voxel during the diffusion time.

Simpler yet, if we assume that the voxel contains a tissue environment that does not vary drastically across this voxel, we can use an even smaller computational domain. This computational domain will only need to contain a "representative" portion of the tissue inside the voxel. Since we would like to study the link between the dMRI signal attenuation and the microscopic scale tissue geometry, such as the cell diameters and the cellular volume fraction, we just need to create computational domains that contain a sample of the cellular configuration that we would like to study. Ideally, numerous samples of the configuration should be simulated to get statistically significant results.

Usually, we constructed meshes of different cellular configurations in a computational domain $C = [-L/2, L/2]^3$ that is on the order of $100\mu m \times 100\mu m \times 100\mu m$. Then we assumed the periodic extension of this computational domain to the whole voxel (and beyond). Inside the computational domain C we define the physical compartments. In the most general case, each compartment corresponds to an individual cell, with an additional compartment being the extra-cellular space (which can be contiguous or not). We can also group all cells of a certain type into a single compartment. We denote the compartments by $\Omega^l, l = 1, 2, 3, \cdots$, $C = \bigcup \Omega^l$, and their associated intrinsic diffusion coefficients by D^l. If all the compartmental intrinsic diffusion coefficients are equal, then we will refer unambiguously to the intrinsic diffusion coefficient, and denote it with a superscript 0, as D^0, where $D^0 = D^l, l = 1, 2, \cdots$ The union of the compartments $\bigcup_{l=1} \Omega^l$ comprises the tissue.

The model for the dMRI signal in the domain C that we will use is the multiple compartment Bloch-Torrey PDE [106, 87]. In the following I will remove the dependence of the MRI signal on the imaging gradients and the T_2 relaxation to isolate the effect of diffusion. The water proton magnetization $M^l(\mathbf{r}, t|\mathbf{g})$ in each tissue compartment Ω^l is subject to :

$$\frac{\partial M^l(\mathbf{r}, t|\mathbf{g})}{\partial t} = -If(t)(\gamma \mathbf{g} \cdot \mathbf{r})\, M^l(\mathbf{r}, t|\mathbf{g}) + \nabla \cdot (D^l \nabla M^l(\mathbf{r}, t|\mathbf{g})), \quad l = 1, 2, \cdots \tag{12}$$

where the parameters are defined previously. When $\mathbf{g} = 0$ this PDE is just a diffusion equation and describes the Brownian motion of water molecules in each compartment. When $\mathbf{g} \neq 0$, between t and $t + \Delta t$, the magnetic field gradient causes the complex transverse magnetization due to water molecules at position $\mathbf{r}$ to gain a complex phase $e^{-I\gamma \mathbf{g} \cdot \mathbf{r} \int_t^{t+\Delta t} f(s) ds}$. Thus, as long as the magnetic field gradient is turned on, the transverse magnetization of water molecules gains a complex phase that is (linearly) related to their spatial positions along their diffusion paths.

We supplement the PDE in (12) with interface conditions where Ω^l and Ω^n come in contact. We denote the interface between Ω^l and Ω^n by Γ^{ln}. One interface condition is the continuity of flux :

$$D^l \left(\nabla M^l(\mathbf{a}, t|\mathbf{g}) \cdot \mathbf{n}^l(\mathbf{a}) \right) = -D^n \left(\nabla M^n(\mathbf{a}, t|\mathbf{g}) \cdot \mathbf{n}^n(\mathbf{a}) \right), \mathbf{a} \in \Gamma^{ln}, \tag{13}$$

where $\mathbf{n}^l(\mathbf{a})$ and $\mathbf{n}^n(\mathbf{a})$ are the *outward*-point normals to Ω^l and Ω^n at $\mathbf{a}$, so in fact $\mathbf{n}^l(\mathbf{a}) = -\mathbf{n}^n(\mathbf{a})$. This ensures the conservation of the magnetization. The second inter-

face condition is :

$$D^l \left(\nabla M^l(\mathbf{a}, t|\mathbf{g}) \cdot \mathbf{n}^l(\mathbf{a})\right) = \kappa^{ln} \left(M^l(\mathbf{a}, t|\mathbf{g}) - M^n(\mathbf{a}, t|\mathbf{g})\right), \mathbf{a} \in \Gamma^{ln}. \tag{14}$$

This incorporates a permeability coefficient κ^{ln} across Γ^{ln} which models the ease with which water cross the interface. The larger the κ^{ln}, the easier the passage of water. Now we add the initial condition :

$$M(\mathbf{r}, 0|\mathbf{g}) = \rho^l, \mathbf{r} \in \Omega^l, \text{ for } l = 1, 2, \cdots, \tag{15}$$

where ρ^l is the water density in Ω^l. Then, same as [112], we assume the computational domain $C = [-L/2, L/2]^3$ is extended by periodic copies of itself. According to [112], the boundary conditions on ∂C are :

$$M(\mathbf{r}, t)|_{r_k=-L/2} = M(\mathbf{r}, t)|_{r_k=L/2}\, e^{I\,\theta_k(t)}, \quad k = 1, 2, 3, \tag{16}$$

$$\left.\frac{\partial M(\mathbf{r}, t)}{\partial r_k}\right|_{r_k=-L/2} = \left.\frac{\partial M(\mathbf{r}, t)}{\partial r_k}\right|_{r_k=L/2} e^{I\,\theta_k(t)}, \quad k = 1, 2, 3, \tag{17}$$

for each of the faces perpendicular to the three coordinate axes, where $\mathbf{r} = (r_1, r_2, r_3)$ and $\mathbf{g} = (g_1, g_2, g_3)$, and

$$\theta_k(t) = \gamma\, g_k\, L \int_0^t f(s)\, ds.$$

Thus, the complete mathematical problem of the multiple compartment Bloch-Torrey PDE for a representative geometry contained in the computational box C consists of the PDE (12), the interface conditions (13,14), the initial condition (15), and the boundary conditions (16,17).

The dMRI signal attenuation is the integral of the magnetization at echo time TE, summed over all the compartments in C. In fact, we can define the integral of the magnetization for $t < TE$ as well :

$$S(b, t) := \frac{1}{\sum_l \rho^l vol(\Omega^l)} \sum_l \int_{\mathbf{r}\in\Omega^l} M^l(\mathbf{r}, t|\mathbf{g})\, d\mathbf{r}, \tag{18}$$

where the b-value b is given in (10).

In biological tissue, the signal attenuation is not a simple decaying exponential in b, and the slope of the $\log S(b, TE)$ at $b = 0$ is not simply related to the intrinsic diffusion coefficients of the physical compartments. After $S(b, TE)$ is obtained at several different values of b, the slope of the $\log S, TE(b)$ at $b = 0$ is computed and called the "Apparent Diffusion Coefficient". This is the most commonly used contrast in a dMRI picture. In addition, a second derivative of the $\log S(b)$ at $b = 0$ can also be computed and gives rise to a different contrast, called the Apparent Kurtosis[13, 45]. These two quantities are computed for each voxel :

$$ADC_0 := -\frac{\partial \log S}{\partial b}(0, TE), \tag{19}$$

$$AK_0 := 3\frac{\partial^2 \log S}{\partial b^2}(0, TE) \left(\frac{\partial \log S}{\partial b}(0, TE)\right)^{-2}, \tag{20}$$

where we denoted the quantities by ADC_0 and AK_0, respectively, to emphasize that the analytical derivatives of $\log S(b, TE)$ are taken at $b = 0$. The ADC_0 and the AK_0 are interesting because the ADC_0 gives an indication of the mean squared distance traveled by water molecules, averaged over all starting positions, and AK_0 gives an indication of the deviation from Gaussian diffusion. Showing the ADC_0 in each voxel in grayscale is called diffusion-weighted imaging and showing the AK_0 is called Kurtosis imaging.

In this thesis, I will briefly mention our work on the numerical solution of the multiple compartment Bloch-Torrey PDE by coupling a standard Cartesian spatial discretization with an adaptive time discretization using the explicit Runge-Kutta-Chebyshev method, which is more efficient than the Forward Euler time discretization for diffusive-type problems. We used this approach to simulate the diffusion MRI signal arising from the extra-cylindrical compartment in a tissue model of the brain gray matter consisting of cylindrical and spherical cells and illustrate the effect of cell membrane permeability.

I will also describe the macroscopic ODE model that we formulated by homogenization for the integral of the solution of the Bloch-Torrey PDE (12, 13, 14,15, 16,17). We showed by numerical simulations that this ODE model gives a good approximation of the signal of the full PDE model for TE in the range of tens of milliseconds, which are physically realistic times obtainable by dMRI in the brain. (The formulation of the ODE model is described in a preprint. An article containing the numerical simulations is also available as a preprint).

Then I mention the work of two PhD students that I am currently co-advising. Dang Van Nguyen works on the improved numerical solution of the Bloch-Torrey PDE by coupling a finite elements discretization to the RKC method as well as the simulation and analysis of diffusion in neurons. He is funded by an ANR grant (project SIMUDMRI, ANR/COSINUS 2010, Nov 2010-Jan 2014). Hang Tuan Nguyen works on the inversion of the ODE model for the purpose of brain tissue parameters estimation. He is funded by a PhD scholarship from STITS Orsay (Oct 2010-Sept 2013).

I will also describe some future research directions in dMRI. The first is the experimental validation of the PDE model by imaging the ganglia (neuronal network) of the Aplysia (giant sea slug), to be conducted at the MRI center Neurospin. The second is the inclusion of blood flow in the brain micro-vessels in a new PDE model, which is the subject of an ANR grant (project CIACM, US-France Collaboration in Computational Neuroscience, Sept 2013-Feb 2017), with funding for a PhD student. The third is the formulation of a different ODE model valid at shorter diffusion times or in the presence of larger cells. This involves using higher order asymptotics than was done for the current ODE model.

In the last part of the thesis, I included some results on the time integration and the construction of artificial boundary conditions for the wave equation.

Deuxième partie

Time integration for equations with memory

Sommaire

1 Development of the techniques for the diffusion equation

Results reported in

1. *On the numerical solution of the heat equation I : fast solvers in free space*, J.-R. Li, L. Greengard, Journal of Computational Physics, Vol. 226-2, 1 Oct. 2007.
2. *Fast and accurate computation of layer heat potentials*, J.-R. Li, L.Greengard, SIAM Journal on Scientific Computing, Vol 31, 2009. pp. 3847-3860.

The solution of the diffusion (heat) equation in unbounded regions arises as a modeling task in a variety of engineering, scientific, and financial applications. While the most commonly used approaches are based on finite difference (FD) and finite element (FE) methods, these must be coupled to artificial (non-reflecting) boundary conditions imposed on a finite computational domain in order to simulate the effect of diffusion into an infinite medium. These boundary conditions are discussed, for example, in [34, 36, 26, 37, 38]. Here, we describe a mathematically much more straightforward approach, which we will refer to as the Fast Recursive Marching (FRM) method. It is based on evaluating the exact solution of the governing equation, using convolution in space and time with the free-space Green's function. One advantage of this approach is that essentially no convergence theory is required. The error in the solution is simply the quadrature error in evaluating the solution.

We illustrate for the case of the isotropic inhomogeneous heat equation in $\mathbb{R}^d$:

$$\frac{\partial U}{\partial t}(\mathbf{x},t) - \nabla^2 U(\mathbf{x},t) = f(\mathbf{x},t), \quad t > 0, \tag{21}$$

in the absence of physical boundaries, subject to the initial condition

$$U(\mathbf{x},0) = U_0(\mathbf{x}), \quad \mathbf{x} \in \mathbb{R}^d. \tag{22}$$

The functions $f(\mathbf{x},t)$ and $U_0(\mathbf{x})$ are assumed to be compactly supported in the box $B = [-R/2, R/2]^d$, centered at the origin. We also assume that $f(\mathbf{x},t)$ and $U_0(\mathbf{x})$ are k-times differentiable : $f(\mathbf{x},t) \in C^k(B \times [0,T])$ and $U_0(\mathbf{x}) \in C^k(B)$.

From standard potential theory [33, 85], the solution can be written as

$$U(\mathbf{x},t) = \int_{\mathbb{R}^d} G(\mathbf{x}-\mathbf{a},t)\, U_0(\mathbf{a})\, d\mathbf{a} \; + \int_0^t \int_{\mathbb{R}^d} G(\mathbf{x}-\mathbf{a},t-\tau)\, f(\mathbf{a},\tau)\, d\mathbf{a}\, d\tau, \tag{23}$$

where G is the fundamental solution in (1).

We will refer to the first integral in (23) as an *initial potential* and the second integral as a *volume potential*. There is a substantial literature on Green's function methods for problems of diffusion (see, for example, [10]). However, straightforward discretization of the above integrals leads to an enormously expensive numerical scheme - the solution is dependent on the full space-time history of the diffusion process. With N points in the discretization of the domain and M time steps, it is easy to see that $O(N^2M + N^2M^2)$ work is required. Thus, the obvious advantages of the approach (stability, robustness,

and the correctness of the far-field behavior) appear to be overwhelmed by the problems of cost.

While (23) describes the solution to the heat equation (21) and (22), significant advantage can be obtained by considering its Fourier transform. For this, we let

$$\hat{U}(\mathbf{s},t) = \int_{\mathbb{R}^d} e^{i\mathbf{s}\cdot\mathbf{x}} U(\mathbf{x},t)\, d\mathbf{x}\,, \quad U(\mathbf{x},t) = \frac{1}{(2\pi)^d} \int_{\mathbb{R}^d} e^{-i\mathbf{s}\cdot\mathbf{x}} \hat{U}(\mathbf{s},t)\, d\mathbf{s}. \tag{24}$$

It is obvious from (21,22), and well-known, that $\hat{U}(\mathbf{s},t)$ satisfies the ordinary differential equation

$$\frac{d\hat{U}}{dt}(\mathbf{s},t) = -\|\mathbf{s}\|^2 \hat{U}(\mathbf{s},t) + \hat{f}(\mathbf{s},t), \tag{25}$$

where

$$\hat{f}(\mathbf{s},t) = \int_{\mathbb{R}^d} e^{i\mathbf{s}\cdot\mathbf{x}} f(\mathbf{x},t)\, d\mathbf{x}.$$

An elementary calculation shows that

$$\hat{U}(\mathbf{s},t) = e^{-\|\mathbf{s}\|^2 \Delta t} \hat{U}(\mathbf{s},t-\Delta t) + \Phi(\mathbf{s},t,\Delta t), \tag{26}$$

where

$$\Phi(\mathbf{s},t,\Delta t) = \int_{t-\Delta t}^{t} e^{-\|\mathbf{s}\|^2 (t-\tau)} \hat{f}(\mathbf{s},\tau)\, d\tau\,. \tag{27}$$

Thus, in the Fourier domain, history dependence is no longer an issue; $\hat{U}(\mathbf{s},t)$ is simply *damped* and *updated* at each time step, as indicated in (26). While this is not a new observation, it is worth introducing some notation; we will refer to $\Phi(\mathbf{s},t,\Delta t)$ in (27) as the *update integral*.

Why, then, is this not the standard procedure for computing U? The answer is that we need a quadrature rule for (27), we need to compute $\hat{f}(\mathbf{s},t)$ from $f(\mathbf{x},t)$, and we need to compute the inverse transform to obtain $U(\mathbf{x},t)$ from $\hat{U}(\mathbf{s},t)$. The first task is easy, the second is a matter of finding a suitable "fast algorithm", and the third is somewhat subtle. We will address these issues in order.

The update integral (27) can be computed to high order accuracy using a standard product integration approach [19], that is to say, polynomial approximation of $\hat{f}(\mathbf{s},t)$ as a function of time, followed by analytic integration. Linear approximation of $\hat{f}(\mathbf{s},t)$ yields second order accuracy and the rule [32]

$$\Phi(\mathbf{s},t,\Delta t) = W_0(\mathbf{s},\Delta t)\hat{f}(\mathbf{s},t) + W_1(\mathbf{s},\Delta t)\hat{f}(\mathbf{s},t-\Delta t), \tag{28}$$

$$W_0(\mathbf{s},\Delta t) = \frac{e^{-z}-1+z}{z^2}\Delta t, \quad W_1(\mathbf{s},\Delta t) = \frac{1-e^{-z}-ze^{-z}}{z^2}\Delta t\,, \tag{29}$$

where $z = \|\mathbf{s}\|^2 \Delta t$.

Given the quadrature rule (28), we still need to compute $\hat{f}(\mathbf{s},t)$ from the data $f(\mathbf{x},t)$. The same transform, of course, is also required at $t=0$ to compute $\hat{U}(\mathbf{s},0)$ from $U(\mathbf{x},0)$.

Since we have assumed that the data is supported in the box $B = [-R/2, R/2]^d$, the Fourier transform is simply

$$\hat{f}(\mathbf{s}, t) = \int_{-R/2}^{R/2} \cdots \int_{-R/2}^{R/2} e^{i\mathbf{s}\cdot\mathbf{x}} f(\mathbf{x}, t)\, d\mathbf{x}, \tag{30}$$

where $\mathbf{x} = (x_1, ..., x_d),\ \mathbf{s} = (s_1, ..., s_d)$.

While we have not, as yet, determined where $\hat{f}(\mathbf{s}, t)$ is to be computed, let us recall that the source $f(\mathbf{x}, t) \in C^k(B)$. Thus, $\hat{f}(\mathbf{s}, t) = O(\|\mathbf{s}\|^{-k})$ for large $\mathbf{s}$. A straightforward calculation shows that if ϵ is the error tolerance, then evaluation of (30) needs to be done only for $\|\mathbf{s}\| \leq P$, where $P = O(1/\epsilon)^{\frac{1}{k}}$. We will refer to P as the *high-frequency cutoff*. This bounds the oscillatory behavior of the term $e^{i\mathbf{s}\cdot\mathbf{x}}$ in the integrand of (30). Together with the fact that $f(\mathbf{x}, t)$ is smooth, it follows that the trapezoidal rule applied to (30) with N points will yield $O(N^{-k})$ accuracy [19]. The error will begin decaying rapidly once N is of the order $O(PR)$, meaning that the integrand is well-resolved. The same reasoning holds for the initial values $\hat{U}(\mathbf{s}, 0)$. If $f(\mathbf{x}, t)$ is given on a uniform mesh with N points in each dimension, the trapezoidal rule yields

$$\hat{f}(\mathbf{s}, t) \approx \left(\frac{R}{N}\right)^d \sum_{n_1=1}^{N} \cdots \sum_{n_d=1}^{N} e^{i\mathbf{s}\cdot\mathbf{x}_n} f(\mathbf{x}_n, t), \tag{31}$$

where $\mathbf{x}_n = \big(-R/2 + n_1(R/N), \ldots, -R/2 + n_d(R/N)\big)$.

It remains only to determine the actual nodes in the Fourier domain $\mathbf{s}_j$ where we wish to obtain $\hat{f}(\mathbf{s}_j, t)$ and, therefore, $\hat{U}(\mathbf{s}_j, t)$.

In order to compute the solution in physical space, we need to evaluate the inverse Fourier transform

$$U(\mathbf{x}, t) = \frac{1}{(2\pi)^d} \int_{\mathbb{R}^d} e^{-i\mathbf{s}\cdot\mathbf{x}} \hat{U}(\mathbf{s}, t)\, d\mathbf{s}\,. \tag{32}$$

Thus, we need to devise a quadrature for (32).

As discussed above, since the data are smooth, we are justified in truncating the domain of integration in the Fourier domain at $\|\mathbf{s}\| = P = O(1/\epsilon)^{\frac{1}{k}}$, with an error ϵ. (If the data were band-limited at frequency P, of course, then this truncation would introduce no error.) The real difficulty lies in developing an efficient rule for the finite Fourier integral :

$$U(\mathbf{x}, t) \approx \frac{1}{(2\pi)^d} \int_{\|\mathbf{s}\|<P} e^{-i\mathbf{s}\cdot\mathbf{x}} \hat{U}(\mathbf{s}, t)\, d\mathbf{s}. \tag{33}$$

The problem of discretizing (33) was addressed in [31], where it was shown (in one dimension) that a mesh which clustered toward the origin in s-space on dyadic intervals was capable of resolving the integrand for all time to any desired precision ϵ. Intuitively, the reason for this exponential clustering at the origin can be understood from considering the Fourier transform of the free space Green's function $\frac{e^{-\|\mathbf{x}\|^2/4t}}{(4\pi t)^{\frac{d}{2}}}$ itself, namely the function $e^{-\|\mathbf{s}\|^2 t}$. For large t, this function is sharply peaked near $\mathbf{s} = 0$ and

the accurate resolution of this function is what ensures that the lowest frequency terms diffuse into the infinite region correctly.

A slight modification of Theorem 2.1 in [31] yields

Theorem 1 *(adapted from [31]) Let $[a,b]$ be a dyadic interval of the form $[2^j, 2^{j+1}]$, let $\epsilon > 0$ be the desired precision and let $\{s_1, \ldots, s_n\}$ and $\{w_1, \ldots, w_n\}$ be the nodes and weights for the n-point Gauss-Legendre quadrature scaled to $[a,b]$. Then,*

$$\left| \int_a^b e^{isx}\, \hat{U}(s,t)\, ds - \sum_{k=1}^{n} e^{is_k x}\, \hat{U}(s_k,t)\, w_k \right| \leq \sqrt{2\pi} \frac{(b-a)}{\sqrt{n}} \left[\frac{R\,(b-a)}{2n} + \sqrt{\frac{\log(1/\epsilon)}{n}} \right]^{2n} + \; O(\epsilon) \tag{34}$$

for $|x| \leq R$.

Note that, in the estimate (34), both terms in square brackets must be small for the quadrature to be accurate. For the first term to be small, the number of nodes must scale like the length of the interval in s-space. The second term is more interesting. It requires that there be at least a constant number of nodes on each interval, *no matter how small*. It is this requirement that forces the exponential clustering of nodes toward the origin.

Corollary 1 *(adapted from [31]) Let $\epsilon > 0$ be the desired precision, let $L_{min} = -\log(1/\epsilon)$ and let $L_{max} = \lceil \log P \rceil$, where P is the high-frequency cutoff. Further, let $\{s_{j,1}, \ldots, s_{j,n(j)}\}$ and $\{w_{j,1}, \ldots, w_{j,n(j)}\}$ be the nodes and weights for the $n(j)$-point Gauss-Legendre quadrature on the interval $[2^j, 2^{j+1}]$, where $n(j) = \max(R\,2^{j+3/2}, 8\log(1/\epsilon))$. Then, in one space dimension,*

$$\left| \int_{|s|<P} e^{-is\cdot x} \hat{U}(s,t) ds - \sum_{j=L_{min}}^{L_{max}} \sum_{k=1}^{n(j)} (e^{is_{j,k}x} + e^{-is_{j,k}x})\, \hat{U}(s_{j,k},t)\, w_{j,k} \right| = O(\epsilon) \tag{35}$$

for $|x| \leq R$.

We will denote by $N_1 = N_1(\epsilon, R, P)$ the total number of nodes required in one dimension. Using a tensor product of this one-dimensional rule, $O(N_1^d) = O((\log(1/\epsilon) + RP)^d)$ nodes are required in d dimensions. If the trapezoidal rule were employed for (33), then $O\left(\frac{RP}{\epsilon}\right)^d$ nodes would be required in order to be accurate for all time $t > 0$.

We have described the Fast Recursive Marching (FRM) method, a simple Fourier-based method for the solution of the heat equation in free space with smooth initial data and a smooth source term. It allows for efficient and accurate long-time simulations without the need for artificial boundary conditions on a finite computational domain. The convergence theory can be stated trivially - the error in the solution is the quadrature error in computing the space-time integral (23). The CPU time of the method is nearly

optimal, requiring $O(N^2 M \log N)$ work for M time steps, with N^2 points in the spatial discretization.

To extend the FRM method to boundary value problems with a non-stationary domain Ω_T with boundary Γ_T :

$$\frac{\partial U}{\partial t}(\mathbf{x},t) - \nabla^2 U(\mathbf{x},t) = f(\mathbf{x},t), \quad (\mathbf{x},t) \in \Omega_T = \prod_{\tau=0}^{T} \Omega(\tau), \tag{36}$$

$$U(\mathbf{x},0) = U_0(\mathbf{x}), \qquad \mathbf{x} \in \Omega(0), \tag{37}$$

$$\alpha U(\mathbf{x},t) + \beta \frac{\partial}{\partial n} U(\mathbf{x},t) = g(\mathbf{x},t), \quad (\mathbf{x},t) \in \Gamma_T = \prod_{\tau=0}^{T} \Gamma(\tau), \tag{38}$$

that is, at each time t, $f(\mathbf{x},t)$ is specified in $\Omega(t)$, the boundary condition (38) is imposed on $\Gamma(t)$, and $U(\mathbf{x},t)$ is defined for $\mathbf{x} \in \Omega(t)$, classical potential theory [85, 33] suggests seeking a solution of the form :

$$U(\mathbf{x},t) = \int_{\Omega(0)} G(\mathbf{x}-\mathbf{a},t) U_0(\mathbf{a}) d\mathbf{a} + \int_0^t \int_{\Omega(\tau)} G(\mathbf{x}-\mathbf{a},t-\tau) f(\mathbf{a},\tau)\, d\mathbf{a}\, d\tau + \int_0^t \int_{\Gamma(\tau)} G(\mathbf{x}-\mathbf{a},t-\tau)\sigma(\mathbf{a},\tau) ds_{\mathbf{a}}\, d\tau + \int_0^t \int_{\Gamma(\tau)} \frac{\partial}{\partial n_{\mathbf{a}}} G(\mathbf{x}-\mathbf{a},t-\tau)\mu(\mathbf{a},\tau) ds_{\mathbf{a}}\, d\tau \,, \tag{39}$$

where $\mathbf{n_a}$ is the unit outward normal to $\Gamma(t)$ at $\mathbf{a}$, $\frac{\partial}{\partial n_{\mathbf{a}}}$ denotes the derivative in the normal direction, $ds_{\mathbf{a}}$ is an element of arc length along the boundary, and σ and μ are unknown surface densities defined on Γ_T. We will refer to the first integral in (39) as an *initial potential*, denoted by $G[U_0]$, to the second integral as a *volume potential*, denoted by $V[f]$, to the third integral as a *single layer potential*, denoted by $S[\sigma]$, and to the fourth integral as a *double layer potential*, denoted by $D[\mu]$. From the basic properties of the Green's function, the representation (39) clearly satisfies (36) and (37). It remains only to satisfy the boundary condition (38), for which we have allowed two unknown functions (the surface densities σ and μ). To avoid non-uniqueness issues, we make the simple choice of using the double layer potential alone for Dirichlet problems ($\beta = 0$), and the single layer potential alone for Neumann or Robin problems ($\beta \neq 0$). Other methods, based on Green's identities, yield different formulations [10, 17, 18, 44].

Defining the double layer potential :

$$D^*[\mu](\mathbf{x}^o,t) := \int_0^t \int_{\Gamma(\tau)} \frac{\partial}{\partial n_{\mathbf{a}}} G(\mathbf{x}^o - \mathbf{a}, t-\tau)\ \mu(\mathbf{a},\tau)\ ds_{\mathbf{a}}\ d\tau, \tag{40}$$

the single layer potential,

$$S[\sigma](\mathbf{x}^o,t) := \int_0^t \int_{\Gamma(\tau)} G(\mathbf{x}^o - \mathbf{a}, t-\tau)\ \sigma(\mathbf{a},\tau)\ ds_{\mathbf{a}}\ d\tau, \tag{41}$$

and

$$K^*(\sigma)(\mathbf{x}^o,t) := \int_0^t \int_{\Gamma(\tau)} \frac{\partial}{\partial n_{\mathbf{x}^o}} G(\mathbf{x}^o - \mathbf{a}, t-\tau)\ \sigma(\mathbf{a},\tau)\ ds_{\mathbf{a}}\ d\tau, \tag{42}$$

for $\mathbf{x}^o \in \Gamma(t)$, the boundary conditions lead to integral equations on the layer densities. For the Dirichlet problem ($\alpha = 1$ and $\beta = 0$ in (38)), taking the limit as a point $\mathbf{x} \in \Omega(t)$ approaches a point $\mathbf{x}^o \in \Gamma(t)$, we obtain the integral equation

$$-\frac{1}{2}\mu(\mathbf{x}^o,t) + D^*[\mu](\mathbf{x}^o,t) = g(\mathbf{x}^o,t) - G[U_0](\mathbf{x}^o,t) \quad (\mathbf{x}^o,t) \in \Gamma_T\,. \tag{43}$$

For the Neumann/Robin problem ($\beta \neq 0$ in (38)), we obtain

$$\alpha S[\sigma](\mathbf{x}^o,t) + \frac{\beta}{2}\sigma(\mathbf{x}^o,t) + \beta K^*[\sigma](\mathbf{x}^o,t) = g(\mathbf{x}^o,t) - \alpha G[U_0](\mathbf{x}^o,t) - \beta\frac{\partial}{\partial n_{\mathbf{x}^o}}G[U_0](\mathbf{x}^o,t)\,. \tag{44}$$

The integral equations in (43) and (44) are well-conditioned Volterra equations of the second kind and well suited to iterative solution. If we assume that some discretization rule in time is used with a time step of Δt, there is an obvious need for the efficient evaluation of $S[\sigma]$ and $D[\mu]$ on $\Gamma(t)$ at $t = n\Delta t$, $n = 1, 2, 3, \cdots, N$. Since the Green's function is non-local in both space and time, it is straightforward to see that naive evaluation would require $O(N^2M^2)$ work, where M is the number of points in the spatial discretization of the boundary. The initial potential would require $O(NM^2)$ work.

Following the approach of [31, 32], the first step in the development of these methods is the decomposition of layer potentials into a local part (the most recent contributions in time) and a history part (the most distant contributions in time) :

$$S[\sigma](\mathbf{x}^o,t) := S_L[\sigma,\delta](\mathbf{x}^o,t) + S_H[\sigma,\delta](\mathbf{x}^o,t) \tag{45}$$

where

$$S_L[\sigma,\delta](\mathbf{x},t) := \int_{t-\delta}^{t}\int_{\Gamma(\tau)} G(\mathbf{x}-\mathbf{a},t-\tau)\;\sigma(\mathbf{a},\tau)\;ds_{\mathbf{a}}\;d\tau, \tag{46}$$

and

$$S_H[\sigma,\delta](\mathbf{x},t) := \int_{0}^{t-\delta}\int_{\Gamma(\tau)} G(\mathbf{x}-\mathbf{a},t-\tau)\;\sigma(\mathbf{a},\tau)\;ds_{\mathbf{a}}\;d\tau\,. \tag{47}$$

The decompositions for $D^*[\mu], K^*[\mu]$ are defined in the analogous manner,

$$\begin{aligned} D^*[\mu](\mathbf{x},t) &:= D^*_L[\sigma,\delta](\mathbf{x},t) + D^*_H[\sigma,\delta](\mathbf{x},t) \\ K^*[\sigma,\delta](\mathbf{x},t) &:= K^*_L[\sigma,\delta](\mathbf{x},t) + K^*_H[\sigma,\delta](\mathbf{x},t)\,. \end{aligned}$$

The fast algorithm is based essentially on three observations : 1) the heat kernel has an analytic expression as a Fourier integral, 2) for a fixed δ, the decay of the high frequency components is very rapid, so that the integral can be computed over a finite range in the Fourier domain for any precision ϵ, and 3) for each given frequency in that range, the Fourier transform satisfies a simple recursion in time, eliminating the explicit history dependence of the "physical space" representation. More precisely, if we define the Fourier transform in space of $S_H[\sigma,\delta](\mathbf{x},t)$ by $\widehat{S_H}[\sigma,\delta](\mathbf{s},t)$, then a straightforward calculation [31, 32] shows that each Fourier mode can be updated in time from the formula :

$$\widehat{S_H}[\sigma,\delta](\mathbf{s},t) = e^{-\|\mathbf{s}\|^2\Delta t}\widehat{S_H}[\sigma,\delta](\mathbf{s},t-\Delta t) + \Phi(\mathbf{s},t,\Delta t,\delta),$$

$$\Phi(\mathbf{s},t,\Delta t,\delta) = \int_{t-\delta-\Delta t}^{t-\delta} e^{-\|\mathbf{s}\|^2(t-\tau)}\int_{\Gamma(\tau)} e^{i\,\mathbf{s}\,\cdot\,\mathbf{a}}\;\sigma(\mathbf{a},\tau)\,d\mathbf{s}_{\mathbf{a}}\,d\tau\,.$$

Likewise for the double layer potential.

While the algorithm is somewhat intricate, the end result is that the history part can be evaluated accurately with only $O(NM \log M)$ work. Thus, to complete the evaluation of heat potentials, it remains only to evaluate the local parts $S_L[\sigma,\delta](\mathbf{x}^o,t)$ and

$$D_L^*[\mu,\delta](\mathbf{x}^o,t) = \int_{t-\delta}^{t}\int_{\Gamma(\tau)} \frac{\partial}{\partial n_{\mathbf{a}}} G(\mathbf{x}^o-\mathbf{a},t-\tau)\,\mu(\mathbf{a},\tau)\,d\mathbf{s}_{\mathbf{a}}\,d\tau, \quad (\mathbf{x}^o,t)\in\Gamma_T \tag{48}$$

for $(\mathbf{x}^o,t)\in\Gamma_T$. This calculation turns out to be surprisingly difficult.

$K_L^*[\sigma,\delta](\mathbf{x},t)$ can be treated in the same manner as its adjoint operator $D_L^*[\sigma,\delta](\mathbf{x},t)$, and will not be considered separately.

Remark 1 *Alternative methods for the rapid evaluation of layer heat potentials have been proposed, for example in [70, 69, 99, 104]. In [70, 69], the authors work with the Laplace transform in time of the heat kernel. In [99, 104], the authors develops a hierarchical space-time approximation scheme. While the treatment of the "history part" differs in each case, the local quadrature issues discussed here arise in essentially the same form and need to be addressed by all.*

Suppose first that the boundary is stationary - that is, $\Gamma(t)=\Gamma(0)$. The essential idea is to expand the density, say σ, in the form :

$$\sigma(\mathbf{x},\tau) = \sigma_0(\mathbf{x})+(t-\tau)\,\sigma_1(\mathbf{x})+\frac{1}{2}(t-\tau)^2\,\sigma_2(\mathbf{x})+\cdots+\frac{1}{(k-1)!}(t-\tau)^{k-1}\,\sigma_{k-1}(\mathbf{x})+O((t-\tau)^k)$$

and to change the order of integration.

The single layer potential S_L then takes the form

$$\begin{aligned} S_L[\sigma,\delta](\mathbf{x},t) = \frac{1}{4\pi}\Bigg[&\int_\Gamma G_0(\mathbf{x}-\mathbf{a})\sigma_0(\mathbf{a})\,ds_{\mathbf{a}} + \int_\Gamma G_1(\mathbf{x}-\mathbf{a})\sigma_1(\mathbf{a})\,ds_{\mathbf{a}} + \ldots \\ &+ \frac{1}{(k-1)!}\int_\Gamma G_{k-1}(\mathbf{x}-\mathbf{a})\sigma_{k-1}(\mathbf{a})\,ds_{\mathbf{a}}\Bigg] + O((t-\tau)^{k+1/2}, \end{aligned} \tag{49}$$

with the kernels $G_k(\mathbf{x})$ given by

$$G_k(\mathbf{x}) = \int_{t-\delta}^{t} e^{-\|\mathbf{x}\|^2/4(t-\tau)}(t-\tau)^{k-1}\,d\tau. \tag{50}$$

A straightforward calculation shows that

$$G_k(\mathbf{x}) = \begin{cases} \mathrm{Ei}(1,\frac{r^2}{4\delta}), & k=0, \\ \frac{4\delta e^{-\frac{r^2}{4\delta}} - r^2\mathrm{Ei}(1,\frac{r^2}{4\delta})}{4}, & k=1, \\ \frac{16\delta^2 e^{-\frac{r^2}{4\delta}} - 4r^2\delta e^{-\frac{r^2}{4\delta}} + r^4\delta\mathrm{Ei}(1,\frac{r^2}{4\delta})}{32}, & k=2, \end{cases} \tag{51}$$

where $\mathrm{Ei}(1,x)$ is the exponential integral function :

$$\mathrm{Ei}(1,x) = \int_1^\infty \frac{e^{-xt}}{t}\, dt\,.$$

Moving boundaries are a bit more complicated. The trick is to use the spatial domain at time t for the entire interval $[t-\delta, t]$. We carry this out explicitly for the double layer potential :

$$D_L^*[\mu,\delta](\mathbf{x},t) = \int_{t-\delta}^{t}\int_{\Gamma(\tau)} \frac{e^{-\frac{\|\mathbf{x}-\mathbf{a}(\tau)\|^2}{4(t-\tau)}}}{8\pi(t-\tau)^2}\Big[(\mathbf{x}-\mathbf{a}(\tau))\cdot n_{\mathbf{a}(\tau)}\Big]\,\mu(\mathbf{a}(\tau),\tau)\,d\sigma_{\mathbf{a}(\tau)}\,d\tau, \tag{52}$$

$$= \int_{\Gamma(t)}\int_{t-\delta}^{t} \frac{e^{-\frac{\|\mathbf{x}-\mathbf{a}(t)\|^2}{4(t-\tau)}}}{8\pi(t-\tau)^2}\Big[h(\mathbf{a},\tau)\Big]\,d\tau\,d\sigma_{\mathbf{a}(t)}, \tag{53}$$

where

$$h(\mathbf{a},\tau) := e^{-\frac{\|\mathbf{a}(t)-\mathbf{a}(\tau)\|^2}{4(t-\tau)}} e^{-\frac{2(\mathbf{x}-\mathbf{a}(t))\cdot(\mathbf{a}(t)-\mathbf{a}(\tau))}{4(t-\tau)}} [(\mathbf{x}-\mathbf{a}(\tau))\cdot n_{\mathbf{a}(\tau)}]\,\mu(\mathbf{a}(\tau),\tau)\frac{d\sigma_{\mathbf{a}(\tau)}}{d\sigma_{\mathbf{a}(t)}}. \tag{54}$$

It is this function that is expanded as a Taylor series in time :

$$h(\mathbf{a},\tau) = h_0(\mathbf{a}) + (t-\tau)\,h_1(\mathbf{a}) + \frac{1}{2}(t-\tau)^2\,h_2(\mathbf{a}) + \cdots + \frac{1}{(k-1)!}(t-\tau)^{k-1}\,h_{k-1}(\mathbf{a}) + O((t-\tau)^k)$$

Changing the order of integration yields

$$D_L^*[\mu,\delta](\mathbf{x},t) = \frac{1}{8\pi}\Big[\int_\Gamma G_{-1}(\mathbf{x}-\mathbf{a})h_0(\mathbf{a})\,ds_{\mathbf{a}} + \int_\Gamma G_0(\mathbf{x}-\mathbf{a})h_1(\mathbf{a})\,ds_{\mathbf{a}} + \ldots \tag{55}$$
$$+ \frac{1}{(k-1)!}\int_\Gamma G_{k-2}(\mathbf{x}-\mathbf{a})h_{k-1}(\mathbf{a})\,ds_{\mathbf{a}}\Big] + O((t-\tau)^{k+1/2}.$$

Note that the double layer involves the kernel G_{-1}, which can be computed explicitly from (50) :

$$G_{-1}(\mathbf{x}) = \frac{e^{-\frac{r^2}{4\delta}}}{\pi r^2} \tag{56}$$

It remains only to consider the nature of the spatial singularities in the evaluation of (55). The apparent $\frac{1}{r^2}$ singularity in G_{-1} does not cause problems because it is canceled by the term $(\mathbf{x}-\mathbf{a}(\tau))\cdot n_{\mathbf{a}(\tau)}$ in $h_0(\mathbf{a})$. More precisely,

$$(\mathbf{x}-\mathbf{a}(\tau))\cdot n_{\mathbf{a}(\tau)} \sim -2\,\gamma_{02}(\mathbf{x},t)\,r^2$$

where $\gamma_{02}(\mathbf{x},t)$ is the curvature at $(\mathbf{x},t)$.

The spatial singularity that remains to be dealt with is the logarithmic singularity in the exponential integral function :

$$\mathrm{Ei}(1,z) = -\gamma - \ln(z) + z - \frac{z^2}{4} + O(z^3).$$

This is easily handled using a variety of quadratures [4, 49, 72], all of which are capable of high-order accuracy for integrands of the form

$$f(x)\ln(|x|) + g(x)\,,$$

assuming only that $f(z)$ and $g(z)$ are smooth. Unfortunately, each of the integrals in (49) or (55) involves a different kernel, so that a suitable fast algorithm is required for each. Finally, note that this approach is suitable for target points off the boundary with no essential change (as mentioned above).

The numerical evaluation of single and double layer heat potentials in two dimensions is a surprisingly complicated task. We have shown that neither asymptotics nor partial product integration schemes are robust - both being highly sensitive to geometric features (not described here, see Paper 2 listed in the beginning of this section for details). We have investigated this loss of the expected order of convergence analytically and refer to it as "geometrically-induced stiffness," since it forces the time step Δt to be proportional to Δx^2 under certain conditions. This is a slight misnomer, since in the integral equation context it manifests itself as a form of inaccuracy rather than a loss of stability. As expected, full product integration of the heat kernel results in robust schemes since the error comes only from the approximations made in representing the geometry and the single or double layer densities themselves. We have used a Taylor series formalism here, which works best for orders of accuracy up to six or so.

In order to construct optimal time algorithms, fast algorithms are needed to compute the spatial convolution integrals that arise in (49) and (55). This can be accomplished, for example, by generalized fast multipole methods [29, 113]. Finally, the local quadrature schemes developed here need to be combined with previously developed fast algorithms for the evolution of the "history part" of layer potentials.

2 Applications and extensions

Results reported in

1. *Efficient thermal field computation in phase field models*,
   J.-R. Li, D. Calhoun, L. Brush. Journal of Computational Physics, Volume 228, Issue 24, 20 December 2009, Pages 8945-8957.
2. *A fast time stepping method for evaluating fractional integrals*,
   J.-R. Li, SIAM Journal on Scientific Computing, Vol 31, 2010. pp. 4696-4714.
3. *Efficient solution of a wave equation with fractional order dissipative terms*,
   H. Haddar, J.-R. Li, D. Matignon. Journal of Computational and Applied Mathematics, Volume 234, Issue 6, 15 July 2010, Pages 2003-2010.

2.1 Phase-field model

Freely growing single crystals exhibit a wide range of crystal-melt interface morphologies, including faceted and dendritic structures, and as a result, have been of great interest to the engineering, scientific, and mathematical communities for decades. Researchers have attempted to understand, predict, and control solidification morphologies

which ultimately impact material properties and performance [55]. Crystal growth morphologies have also been a subject of interest to researchers studying nonlinear dynamical systems because freely growing crystals are examples of rich, pattern-forming systems [57, 20].

We consider the solidification of a pure material. The model we use are the phase-field equations, which consist of a coupled system of two diffusion-type equations governing a dimensionless temperature $u(x, y, t)$ (the thermal field) and the phase variable $\phi(x, y, t)$. We use the following formulation of the model equations :

$$u_t - \nabla^2 u = \frac{1}{2\,S}\,(h(\phi))_t\,, \tag{57}$$

$$\tau_0\, a(\theta)^2 \phi_t = \left[\frac{\phi(1-\phi^2)}{D} - \frac{\tau_0\, S}{a_2\, w_0^2}\, u\,(1-\phi^2)^2 + \frac{w_0^2}{D}\,\nabla_a^2(\theta)(\phi)\right], \tag{58}$$

for $\mathbf{x} = (x, y) \in \mathbb{R}^2$, $t > 0$, along with the choice of parameters,

$$h(\phi) = \phi,\ a2 = 0.6267,\ \tau_0 = 1,\ w_0 = 1.$$

The thermal and the phase variables are subject to initial conditions :

$$u(x, y, 0) = u_0(x, y), \quad \mathbf{x} = (x, y) \in \mathbb{R}^2, \tag{59}$$

$$\phi(x, y, 0) = \phi_0(x, y), \quad \mathbf{x} = (x, y) \in \mathbb{R}^2. \tag{60}$$

The normalized temperature is $u = (T - T_M)/\Delta T$, where T_M is the equilibrium melting temperature at a planar interface and ΔT is the melt under-cooling (the difference between the melting temperature and the initial temperature in the bulk liquid). Interfacial properties such as the crystal-melt interface energy and the local atomic attachment coefficient depend on interfacial orientation, i.e. they are anisotropic. In (57-60) the anisotropy of the material properties is included through the anisotropic Laplacian, which depends on the angle θ (for example, the angle that the normal to the iso-ϕ contours makes with the x-axis) :

$$\nabla_a^2(\theta) = -\frac{\partial}{\partial x}\left(a(\theta)a'(\theta)\frac{\partial}{\partial y}\right) + \frac{\partial}{\partial y}\left(a(\theta)a'(\theta)\frac{\partial}{\partial x}\right) + \nabla\cdot\left(a^2(\theta)\nabla\right), \tag{61}$$

with θ computed by the formula

$$\theta = \tan^{-1}\left(\frac{\partial_y \phi}{\partial_x \phi}\right). \tag{62}$$

The anisotropy is typically modeled by

$$a(\theta) = 1 + \epsilon_4 \cos w\,\theta, \tag{63}$$

where ϵ_4 is the strength of the anisotropy and w is the crystalline symmetry (e.g., $w = 4$ for four-fold symmetry).

The phase variable varies from $\phi = -1$ (liquid) to $\phi = 1$ (solid), corresponding to the liquid and solid phases, respectively. The value of ϕ varies smoothly but sharply from -1 to 1 in a narrow diffuse interface region. The Stefan number, or dimensionless undercooling, is given by

$$S = \frac{c\Delta T}{L}, \tag{64}$$

where c is the specific heat per unit volume and L is the latent heat per unit volume. Typical simulations reported in the literature assume S to be in the range $0.05 \sim 1$. However, experimental results often report values of S in the range $0.001 \sim 0.1$ [56].

Regimes of theoretical and experimental importance most easily accessible by numerical computations are those for which the temperature of the liquid melt is relatively far from the equilibrium melting temperature. In such regimes, the non-dimensional undercooling parameter, the Stefan number, is large (typically $O(1)$) and crystals grow fast relative to the expansion of the thermal field. One can observe interesting results before the extent of the thermal field exceeds the computational domain and adequate resolution of the solid-liquid interface can be achieved at modest computational expense. Many of the early dendritic growth calculations reported in the literature were computed in this regime [109, 105, 9, 81, 51, 111, 80].

By contrast, obtaining accurate numerical solutions in the regime of low undercoolings still proves to be computationally challenging. For low Stefan numbers (see Eqn. (64)) crystals grow very slowly relative to the rate of expansion of the thermal front and the extent of the thermal field in the liquid can quickly exceed by several orders of magnitude the size of the growing crystal. Typically, in numerical simulations using finite difference or finite elements methods, the computational domain is taken to be large enough to contain the entire thermal field. This is due to the fact that in order to match experiments, numerical simulations must not exhibit any spurious artifacts introduced by the presence of an artificial computational boundary. The boundary conditions that are almost universally applied because they are easy to implement are purely Neumann conditions (see [81, 9, 90]). This choice of artificial boundary conditions will result in a distorted thermal field at long times and hence an incorrect solution to the free space crystal growth problem.

The field of interest in the phase-field equations is represented by the phase variable. The thermal field is of interest near the dendritic tips but is of only secondary interest away from the crystal interface. For this reason, one would ideally like to use a computational domain for u which is the same size as needed for ϕ even at low undercoolings. We want the thermal field to diffuse out through the computational boundary as if the boundary were not there.

We used the Fast Recursive Marching (FRM) method described in the previous section to compute the thermal field. Using this approach, we eliminate the need for artificial boundary conditions for the thermal field because we use a form of the solution that automatically satisfies the correct boundary conditions on the computational domain. In other words, these conditions do not need to be artificially imposed. For the second equation of the phase field model, the phase equation, we will use the Runge-Kutta-Chebyshev (RKC) method [95] (specially formulated for the time integration of parabolic PDEs discretized by the method of lines). The RKC method is an explicit method that computes the solution of moderately stiff problems with a small of number of stages and function evaluations while ensuring stability. Although the equation for ϕ also appears to be a diffusion-type equation, in fact, it is not a true diffusion equation. This can be seen by writing the term $\nabla_a(\theta)\nabla\phi$ in tensor notation as $\nabla L(\theta)\nabla\phi$ and noting that the resulting anisotropic tensor $L(\theta)$ is skew symmetric, with complex eigenvalues, and so does not behave as a true diffusion tensor [109]. As a consequence, the field for ϕ does not extend beyond the interface and is constant outside of this region.

The *adaptive* computational domain will be denoted Ω^t, which contains the support of ϕ. It is clear from (57) that this means that Ω^t will always contain the source for u.

Snapshots of the crystal at various time points for the low undercooling case, $S = 0.025$ and $D = 400$, are plotted in Figure 3. The crystal and the thermal field are shown inside the computational domain Ω^t at each time point. The computational domain Ω^t enlarges from $[-10, 10] \times [-10, 10]$ at $t = 0$ to $[-256, 256] \times [-256, 256]$ at $t = 600000$. In contrast to finite difference/elements methods where one must enlarge Ω^t as soon as the support of $u(\cdot, \cdot, t)$ approaches $\partial\Omega^t$, in our approach, we do not have to enlarge Ω^t until the support of $\phi(\cdot, \cdot, t)$ approaches $\partial\Omega^t$, a great advantage at low undercoolings. In Figure 4 we show the support of the thermal field at $t = 300000$ which is much larger than the computational domain we used ($[-174, 174] \times [-174, 174]$ at $t = 300000$).

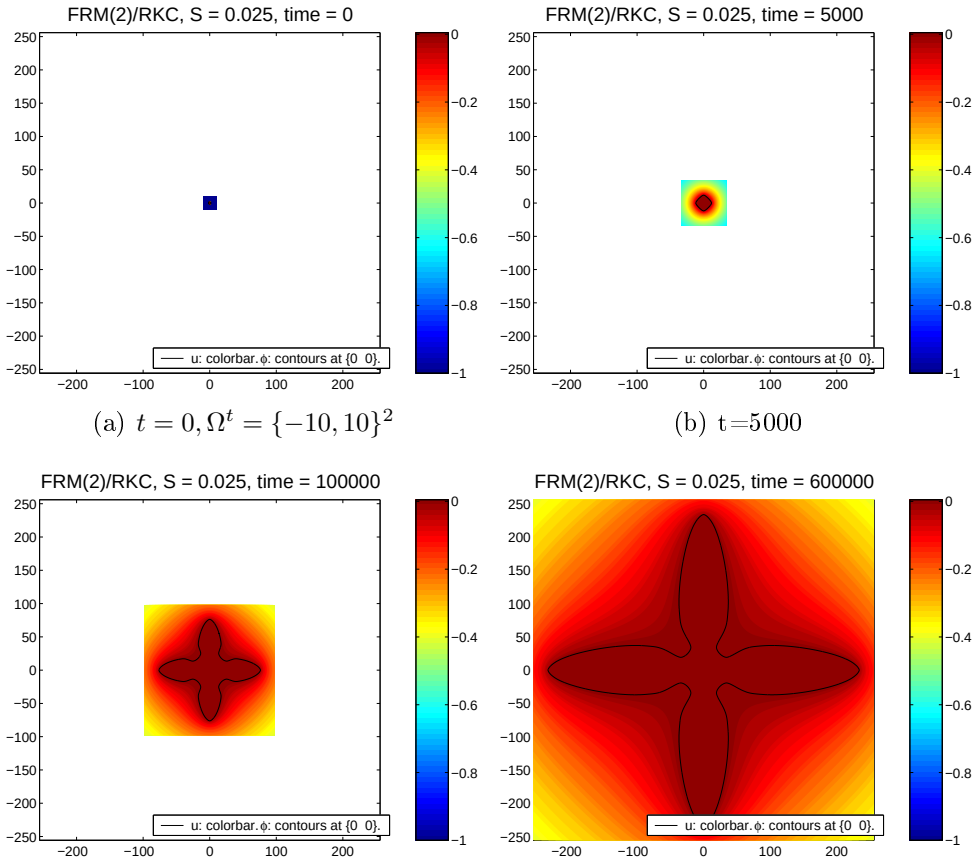

(a) $t = 0, \Omega^t = \{-10, 10\}^2$ (b) t=5000

(c) t=100000 (d) $t = 600000, \Omega^t = \{-256, 256\}^2$.

FIG. 3 – The thermal field and phase plotted on the adaptive computational domain Ω^t. The thermal field is computed via the FRM method. The phase is computed via the RKC method. When the thermal field is computed with the FRM method heat diffuses out of Ω^t correctly and simulation can continue until the solidification front reaches $\partial\Omega^t$.

While we have demonstrated our solver on the phase-field equations, it can also be incorporated into solvers for the sharp interface model. This would involve solving an initial boundary value heat equation instead of the free space heat equation with a source term.

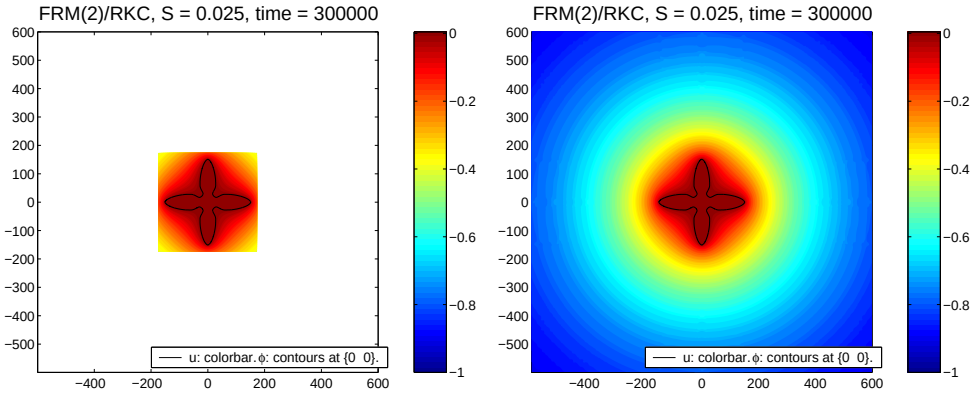

(a) Computational domain of FRM/RKC method.

(b) Thermal field.

FIG. 4 – The computational domain required by the FRM/RKC method can be much smaller than the thermal field. Competing finite difference or finite elements methods require a computational domain that contains the entire thermal field.

2.2 Fractional integrals

In recent years models have come from physical applications that involve fractional (non-integer) order integrals and derivatives [67, 21, 12, 84]. Numerical methods for the evaluation of fractional order integrals and the solution of fractional order differential equations can be found in numerous papers (an early work is in [68], a recent survey can be found in [22]). In the iterative solution of fractional order differential equations, one is led to the repeated evaluation of fractional order integrals, which will be the focus of this work.

We seek to evaluate the fractional integral of order α,

$$I^{\alpha}[f](t) := \frac{1}{\Gamma(\alpha)} \int_0^t (t-\tau)^{\alpha-1} f(\tau)\, d\tau, \quad 0 < \alpha < 1, \tag{65}$$

at time steps $t = \Delta t, 2\Delta t, \cdots$, for smooth and nonsmooth f. We have in mind that this is a part of the simulation process of a dynamical model. One may want to simulate this model for very long times, and the final time of simulation may not be fixed a priori.

The principle difficulty in evaluating (65) for long times is that the convolution kernel $t^{\alpha-1}$ decays slowly for large t. Hence, to compute $I^{\alpha}[f](t)$ the contribution due to $f(\tau)$ for τ far away from t cannot be neglected. This is the reason that systems which contain terms like $I^{\alpha}[f](t)$ are said to have memory. Hence, a naive discretization of (65)

$$I^{\alpha}[f](n\Delta t) \approx \sum_{j=0}^{n} c_{nj} f(j\Delta t),$$

gives rise to an algorithmic complexity which is quadratic in the number of time steps, because the coefficients c_{nj} changes with the time step n, reflecting the fact that $(t-\tau)^{\alpha-1}$ depends on t.

An additional complication comes from the fact that the input function f may have an integrable end point singularity : in the solution of fractional order differential equations, the input function will be the solution obtained up to the current time step, and

it will be a sum of terms of the form :

$$\left\{t^{\beta},\ \beta = j + l\alpha,\ j, l \in \{0, 1, 2, \cdots\}\right\}. \tag{66}$$

In a classical approach ([68] and later works) the fractional integral in (65) is approximated as the sum of a discrete convolution and a few correction terms :

$$\frac{1}{\Gamma(\alpha)} \int_0^{n\Delta t} (n\Delta t - \tau)^{\alpha-1} f(\tau) d\tau \approx \Delta t^{\alpha} \sum_{j=0}^{n} \omega_{n-j} f(j\Delta t) + \Delta t^{\alpha} \sum_{j=0}^{s} w_{nj} f(j\Delta t), \quad n = 1, 2, \cdots N. \tag{67}$$

The convolution weights ω_j, $j = 0, \cdots, N$, are obtained as the Taylor expansion coefficients of the generating function, taken to the power α, of a linear multistep method for first order ODEs (for example, Euler, BDF). For a fixed N, they can be computed via the Fast Fourier Transform. The weights of the correction terms w_{nj}, $n = 1, \cdots, N$, $j = 1, \cdots, s$ are the solution of a generalized Vandermonde linear system, obtained by requiring that s functions with the lowest powers in the set described by (66) satisfy (67) exactly. This system is ill-conditioned and it must be solved at each time step n (see [24] for further details). Suppose the weights ω_j, $j = 0, \cdots, N$, and w_{nj}, $n = 1, \cdots, N$, $j = 1, \cdots, s$, have been thus obtained. The sum in (67) can be computed for $n = 1, \cdots, N$, in $O(N(\log N)^2)$ complexity with $O(N)$ storage, by properly ordering the computations on the triangle $\{(t, \tau) : 0 \le \tau \le t \le T\}$ and using the Fast Fourier Transform [35].

In another group of works the model containing the fractional integral is reformulated as a system of differential equations by taking advantage of a particular integral representation of the convolution kernel $t^{\alpha-1}$:

$$t^{\alpha-1} = \frac{1}{\Gamma(1-\alpha)} \int_0^{\infty} e^{-\xi t} \xi^{-\alpha} \, d\xi. \tag{68}$$

This or a similar representation was used for the purpose of analysis in [96, 77, 75, 78] and for the purpose of numerical simulation in [114, 15, 78, 41]. The numerical algorithms suggested by [114] and [15], which are very similar, were used in [107, 114, 67] and analyzed and criticized in [93, 67, 23].

The numerical algorithms formulated in [114, 15, 78, 41] all required a good discretization of (68), i.e., an efficient and accurate quadrature for the function $e^{-\xi t}\xi^{-\alpha}$ on the half line $[0, \infty)$. The principle difficulty with this problem lies in the fact that $e^{-\xi t}\xi^{-\alpha}$ depends on t but the quadrature, ideally, should not depend on t. In [78, 41] a quadrature involving logarithmically spaced nodes was proposed. In [114] and other papers that use the method proposed there, generalized Gaussian type quadratures (Gauss-Laguerre for the weight function e^{-x}, Gauss-Jacobi for a weight function containing fractional order end point singularities) were suggested.

We believe the major default of these previous works is that the authors attempted to find a quadrature that is accurate for all $t \in [0, \infty)$ or for all $t \in [0, T_{max}]$, which is an impossible task, given that the integral does not converge at $t = 0$. This can be clearly seen in the singularity of $t^{\alpha-1}$ at $t = 0$. Hence, in our work, we limit the use of the integral representation in (68) to t which is at least Δt away from 0. We present a quadrature which is efficient and accurate to within a given error tolerance for *all* $t \in [\Delta t, \infty)$.

The idea that an integral representation should only be used for $t \geq \Delta t$ is included in another set of works [71, 92, 66]. But these works use a substantially different integral representation, in fact, a complex contour integral. For the case of the kernel $t^{\alpha-1}$ this representation is

$$t^{\alpha-1} = \Gamma(\alpha)\, \frac{1}{2\pi i} \int_{\Lambda} e^{\xi\, t} \xi^{-\alpha} d\xi, \tag{69}$$

where Λ is a contour in the complex plane in the region of analycity. Those authors were not able to find one unique quadrature set for (69) that is accurate for all $t \in [0, T_{max}]$ so they divided $[0, T_{max}]$ into geometrically growing and overlapping intervals $\bigcup_l [B^{l-1}\Delta t, B^{l+1}\Delta t]$ for some $B > 1$, and a different quadrature (on a different contour) is used for each interval $[B^{l-1}\Delta t, B^{l+1}\Delta t]$. This leads to a complicated time stepping strategy because all quadrature nodes must be advanced at every time step. Clearly, it is also necessary to selectively store and delete of the 'past' values of f to keep the storage requirement down. However, because the quadrature sets depend t, if one decides during the course of simulation to continue past T_{max}, additional quadrature sets for further time intervals must be advanced from the beginning. If the values of the input function f for the earlier times were not stored, then they need to be recomputed. The advantage of this approach is that it can be used for a more general class of kernels, but for the particular case of $t^{\alpha-1}$, we believe the method we propose is superior.

We will formulate one quadrature set that is accurate to a tolerance ϵ for the entire interval $[\Delta t, \infty)$, there is no limitation on T_{max} so simulation can continue as long as needed. We show that the number of points in the quadrature set, Q, is $O\left(\left(-\log\epsilon - \log\Delta t\right)^2\right)$. The complexity of our algorithm is then $O(N\,Q)$, where N is the number of time steps, and the storage is $O(Q)$. Because Q does not depend on N, the number of time steps do not need to be fixed a priori to achieve linear algorithmic complexity.

This work is motivated by the approach taken in [31] where a quadrature set is generated for the heat kernel ($\alpha = \frac{1}{2}$) which is valid for $[\Delta t, \infty)$. Here we compute quadratures valid for other values of α and give a complete analysis of the quadrature error and a different bound on Q. We show explicitly how these quantities depend on α. In addition, we treat the case of input functions f which may have an end point singularity at $t = 0$.

We proved the following theorem concerning our proposed quadrature.

Theorem 2.1 *The quadrature with nodes* $\{\eta^1, \cdots, \eta^Q\}$ *and weights :* $\{v^1, \cdots, v^Q\}$ *satisfies the following error bound*

$$\left| \frac{1}{\Gamma(1-\alpha)} \int_0^\infty e^{-\xi\, t} \xi^{-\alpha}\, d\xi - \frac{1}{\Gamma(1-\alpha)(1-\alpha)} \sum_{k=1}^{Q} e^{-(\eta^k)^\gamma\, t}\, v^k \right| \leq \epsilon, \quad \forall t \in [\Delta t, \infty),$$

with the number of quadrature nodes Q *satisfying the asymptotic bound*

$$Q = O\left(\frac{(-\log\epsilon - \log\Delta t)^2}{2\log\left(\rho_{max}(\gamma)\right)} \right),$$

where

$$\gamma = \frac{1}{1-\alpha}, \rho_{max}(\gamma) := \sqrt{\frac{17w^2 + 1 + 4\sqrt{18w^4 + 2w^2}}{w^2 + 1}}, w := \tan\frac{\pi}{2\gamma}.$$

The proof of the theorem can be found in Paper 2 listed at the beginning of this section.

We presented a method of evaluating fractional integrals by using an efficient quadrature of the integral representation of the convolution kernel $t^{\alpha-1}$. This quadrature is to be used as a part of a fast time stepping method. The new method has algorithmic complexity $O(NQ)$ and storage requirement $O(Q)$, where N is the number of time steps and Q is the number of nodes in the quadrature. We have shown that Q is independent of N and grows as $O\left(\left(-\log\epsilon-\log\Delta t\right)^2\right)$, where ϵ is the quadrature error tolerance and Δt is the size of the time step. The possible end point singularity of the input function is taken into account by this algorithm.

2.3 Fractional wave equation

The dissipative model that describes acoustic waves traveling in a duct with viscothermal losses at the lateral walls is a wave equation with spatially-varying coefficients that involves fractional-order integrals and derivatives. The main goal of this work is to propose an efficient numerical discretization of the coupled model that, in particular, would avoid storing the solution from all the past time steps, because that would be too computationally penalizing in long time simulations.

Our approach is based on the so-called diffusive representations of the fractional integral where, roughly speaking, the fractional-order time kernel in the integral is represented by its Laplace transform. This allows for efficient time domain discretization because the value of the integral at each time step can be updated from the value at the previous time step by operations which are local in time (contrary to a naive discretization of the fractional integral where global-in-time operations are required). However, these representations require the evaluation of an integral over the Laplace variable domain. We propose a numerical method that provides uniform control of the accuracy with respect to the simulation time. The idea of this approach is inspired by the work in [31] and follows the detailed development in [64] : the convolution integral is split into a local part and a historical part, where for the latter one can exploit the exponential decay of the Laplace kernels to choose quadrature rules that provide uniform error bounds in time. Essentially, the number of quadrature points in the Laplace domain is $O(-\log(\Delta t))$ where Δt denotes the time step. Thus, if M is the number of time steps, the numerical scheme we propose requires $O(M\log(M))$ work and $O(\log(M))$ memory, compared to $O(M^2)$ work and $O(M)$ memory of a naive discretization.

We focus on the one-dimensional Webster-Lokshin model in a simplified form

$$\partial_t^2 w + a(z)\partial_t^{2-\beta} w + b(z)\partial_t w - \frac{1}{r^2(z)}\partial_z(r^2(z)\partial_z w) = 0, \tag{70}$$

for $t>0$ and $z\in[0,1]$, where $\beta\in(0,1)$, $r,a,b\in L^\infty([0,1];\mathbb{R}^+)$; the radius of the duct satisfies $r\geq r_0>0$. The Riemann-Liouville fractional integral operator $\partial_t^{-\beta}$ is defined by

$$(\partial_t^{-\beta} f)(t) := \frac{1}{\Gamma(\beta)}\int_0^t \frac{f(\tau)}{(t-\tau)^{1-\beta}}\,d\tau. \tag{71}$$

Working with $(p,\, v) := (\partial_t w,\, -r^2(z)\,\partial_z w)$ leads to the first order system :

$$\partial_t p = -r^{-2}\,\partial_z v - b\,p - a\,\partial_t^{-\beta}(\partial_t p)\ , \tag{72}$$
$$\partial_t v = -r^2\,\partial_z p\ , \tag{73}$$

which we supplement with the boundary conditions :

$$p_0(t) := p(z=0,\, t) = u(t)\ , \tag{74}$$
$$v_1(t) := v(z=1,\, t) = 0. \tag{75}$$

We assume initial values and are interested in the relation between input $u(t) = p(z = 0,\, t)$ and output $y(t) = p(z = 1,\, t)$. More general models allow for a $c(z)\,\partial_t^{1-\beta'} w$ term in (70), as well as boundary conditions of the impedance type instead of (74-75), both at $z = 0$ and $z = 1$. The additional term can be treated in a similar manner as $\partial_t^{2-\beta} w$.

The main idea is the representation of the convolution kernel as an integral of a family of decaying exponentials with respect to a positive measure. In other words, we utilize the following identity :

$$\frac{1}{\Gamma(\beta)}\frac{1}{(t-\tau)^{1-\beta}} = G_\beta \int_0^\infty e^{-\xi\,(t-\tau)}\xi^{-\beta}\,d\xi, \tag{76}$$

where $G_\beta := \frac{1}{\Gamma(\beta)\Gamma(1-\beta)} = \frac{\sin\beta\pi}{\pi}$, which in essence states that the convolution kernel in (71) is the inverse Laplace transform of $G_\beta\,\xi^{-\beta}$.

One can easily check that the dynamical system with input $f \in L^2([0,T])$ and output $\theta^{[\beta]}(f) \in L^2([0,T])$:

$$\partial_t\varphi(\xi,t) = -\xi\varphi(\xi,t) + f(t),\ \forall\xi\in\mathbb{R}^+, \tag{77}$$
$$\theta^{[\beta]}(f)(t) = G_\beta \int_0^\infty \varphi(\xi,t)\,\xi^{-\beta}\ d\xi, \tag{78}$$

given $\varphi(\xi,0) = 0$, provides a (diffusive) realization of the fractional integral $\partial_t^{-\beta}$; in other words, (77-78) realizes the input-output relation $\theta^{[\beta]}(f) = \partial_t^{-\beta} f$. It is clear that the state φ is such that $E_\varphi := \frac{G_\beta}{2}\int_0^\infty |\varphi|^2\,\xi^{-\beta}\,d\xi < \infty$.

We designed a numerical scheme which avoids the storage of the entire history of past data and that provides uniform control of the accuracy. We observed numerically that it is stable under the standard CFL condition, however, no discrete energy balance has been yet found for it. Details of this method can be found in Paper 3 listed at the beginning of this section.

Troisième partie

Modeling and simulation of diffusion magnetic resonance imaging in the brain

Sommaire

3 Scientific context of diffusion magnetic resonance imaging

A major application of diffusion magnetic resonance imaging has been in acute cerebral ischemia (stroke) [79, 110]. DMRI has been used to detect and differentiate a wide range of physiological and pathological conditions, including, in the brain, tumors [101, 108, 74], myelination abnormalities (for a review, see [60]), as well as in the study of brain connectivity (for a review, see [58]) and in functional imaging [61].

Algorithms that attempt to quantify tissue microstructure from the measured dMRI signals developed alongside the clinical applications, and impressive progress has been made in quantifying white matter fibers (see[58] for a review). This is because white matter is made of bundles of myelinated axons (myelin is an insulating layer surrounding the axon of a neuron) that, at the level of the spatial resolution of dMRI, are (mostly) aligned in some predominate direction. These axons can be modeled by cylinders with impermeable membranes. The models of the dMRI signal in the white matter[94, 5] thus rely on adding up the contributions of the signals from water inside the cylinders and water outside the cylinders, with no water exchange between the cylinders and the space outside. This is a mathematical tractable problem because diffusion solutions inside impermeable cylinders can be obtained analytically and added over a distribution of spatial orientations. The diffusion in the space outside the cylinders can be assumed to be Gaussian, with a possibly anisotropic effective diffusion tensor.

In the brain gray matter, analogous models have not been as successful because the cell dimensions are much smaller : the imaging voxel contains neurons and not just the axons. At the level of the spatial resolution of dMRI, the signal is averaged over many neurons, consisting of round neuronal bodies attached to long protrusions called neurites (axons and branching dendrites). Very importantly, the cells (neurons and glial cells) are permeable to water, including the axons that are mostly unmyelinated. For example, when impermeable cylindrical sticks were used to model neurons for dMRI in[46] it was found that such a model allows an accurate estimation of myelinated axon density in the gray matter, but not the dendrite density. This result is not surprising because water exchange through cell membranes in the gray matter is important and should not be neglected.

If water passes very slowly between the cells and the extra-cellular space compared to the measured diffusion time, then the cell membranes can be approximated as impermeable to water passage. In this case, various analytical or semi-analytical expressions have been obtained for the dMRI signal arising from *inside* the cells [98, 11, 83, 87, 102, 30]. In general, however, cell membranes are permeable to water, and it is important to study the effect of membrane permeability on dMRI signals. If the cell membranes are permeable, analytical solutions are not known even for these simple geometries. One needs thus to resort to numerical simulation as well as to macroscopic models.

4 Numerical solution of a microscopic PDE model

Results reported in

1. *Numerical simulation of diffusion MRI signals using an adaptive time-stepping method*,
   J.-R. Li, D. Calhoun, C. Poupon, D. Le Bihan. Accepted. Physics in Medicine and Biology, 2013.

We solved the multiple compartment Bloch-Torrey PDE by coupling a standard Cartesian spatial discretization with an adaptive time discretization using the explicit Runge-Kutta-Chebyshev (RKC) method, which is more efficient than the the Forward Euler time discretization used previously for dMRI simulations [43, 48, 112, 40, 91].

In the brain gray matter, neurons, consisting of a large neuronal body and long extensions (axons and dendrites), are densely packed. There are also glial cells which do not have these long extensions. The extra-cellular space accounts for only a small fraction of the total volume, less than 20 percent. In [47], a simplified model of the dMRI signal was proposed :

$$S(b) = (1 - v^c)\, e^{-D^{ec} b} + v^c S^c(b), \tag{79}$$

where v^c is the volume fraction of all the diffusion compartments exhibiting cylindrical symmetry and everything outside of these cylindrical compartments is assumed to undergo Gaussian diffusion with an *effective* diffusion coefficient D^{ec}, where the superscript "ec" stands for "extra-cylindrical". The term $S^c(b)$ is the signal due to the cylindrical compartments under the assumption that they are *impermeable* with respect to the extra-cylindrical compartment. In the gray matter, where there is no a-priori orientation preference for the neurites (axons and dendrites), the cylindrical compartments consist of the neurites themselves. We are interested in simulating the dMRI signal from regions of the brain where the neurites can be thought of as oriented more or less *randomly*.

First we studied the dMRI signal arising from the compartment consisting of the extra-cellular space and the spherical cells (modeling glial cells). We begin by constructing a geometry consisting of generally oriented cylinders and spheres. In the computational box $C = [-12.5\mu m, 12.5\mu m]^3$, we placed $N^c = 250$ randomly-placed points (uniformly distributed in C). At each point, we extended an infinite cylinder of radius R^c oriented in a random direction (drawn uniformly from the unit sphere) and cut the cylinder off at the boundaries of C. The size of C is chosen for the simulation of the extra-cylindrical space, where we observed that the effective diffusion coefficient was no more than $10^{-3} mm^2/s$, meaning a diffusion distance of $15\mu m$ in $40ms$. This size ensures that most molecules see C no more than twice during $40ms$. The cylindrical volume fraction will be denoted v^c. We also distribute $N^s = 10$ randomly-placed spheres of radius R^s in C and denote the spherical cells volume fraction by v^s. The volume fraction of the extra-cellular space will be denoted $v^e = 1 - v^c - v^s$. See Fig 5(a) for a rendering of the geometry with $R^c = 1.25\mu m$, $R^s = 4\mu m$, $v^e = 0.15$ and $v^s = 0.15$. We discretized C by a regular mesh with spatial spacing h. See Fig 5(b) for a cross section view of the discretized mesh at $h = 0.125\mu m$.

At the start of the simulation, we placed water molecules uniformly in the spherical cells and the extra-cellular space and placed no water molecules inside the cylinders. We

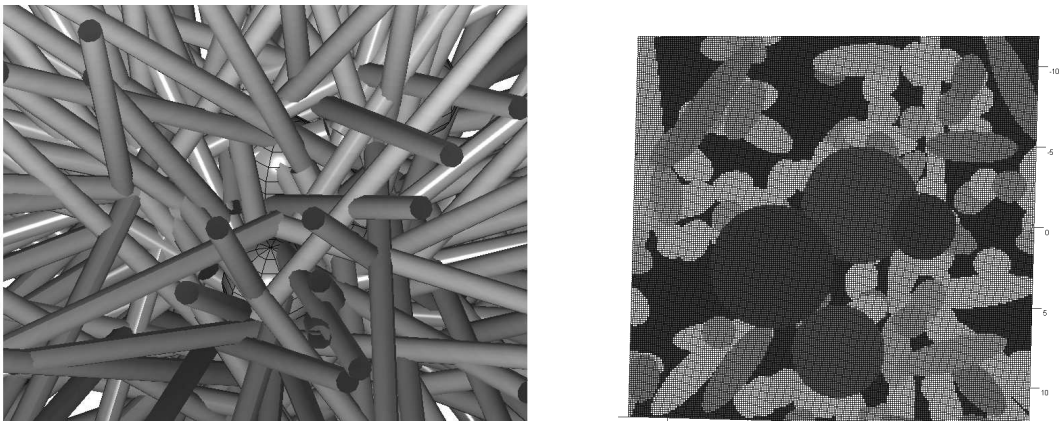

(a) Geometry (b) Cross section of mesh

FIG. 5 – Left : a rendering of the simulation geometry consisting of 250 randomly placed and oriented cylinders and 10 randomly placed spheres (zoomed-in view). Right : a cross section view of the discretized mesh of the geometry with $h = 0.125\mu m$ (zoomed-in view).

made the cylindrical cells *impermeable* so that the water molecules are blocked from entering the cylinders during the simulation. We varied the spherical cell permeability : $\kappa^s = 0m/s$(impermeable), $10^{-5}m/s, 10^{-4}m/s, \infty$(infinitely permeable), and we computed the ADC_0 and AK_0 from b-values : $0, 250, 500, 750, 1000, 1250, 1500, 1750, 2000s/mm^2$. The RKC tolerance was set to $tol = 10^{-4}$, after doing a preliminary simulation for free diffusion where we saw that the relative signal error was less than 0.005 at $b = 2000s/mm^2$, which is sufficient accuracy for the dMRI application where there is significant experimental noise in the measured signal.

We chose a constant intrinsic diffusion coefficient $D^0 = 3 \times 10^{-3}mm^2/s$ in the cells and the extra-cellular space. The diffusion-encoding gradient sequence simulated was PGSE, $\delta = 2.5ms$ and we varied $\Delta = 10ms, 20ms, 30ms, 40ms$. We simulated the dMRI signal on two meshes with $h = 0.25\mu m$ and $h = 0.125\mu m$.

We examine the results for the mesh with $h = 0.125\mu m$ (marked by stars). In Fig. 6, we see that at $\kappa^s = 0m/s$ (solid line) and $\kappa^s = 10^{-5}m/s$ (dash-dots), the ADC_0 decreases from $0.4 \times 10^{-3}mm^2/s$ to $0.2 \times 10^{-3}mm^2/s$ as the diffusion time is increased from $10ms$ to $40ms$, while the AK_0 goes from 1.8 to 2.7 for $\kappa^s = 10^{-5}m/s$ and from 2 to 3.5 for $\kappa^s = 0m/s$. At $\kappa^s = 10^{-4}m/s$ (dashes), the ADC_0 decreases from $0.55 \times 10^{-3}mm^2/s$ to $0.45 \times 10^{-3}mm^2/s$, while the AK_0 stays around 1.2. At $\kappa^s = \infty m/s$ (dots), the ADC_0 decreases from $1.05 \times 10^{-3}mm^2/s$ to $0.85 \times 10^{-3}mm^2/s$, while the AK_0 stays around 0.6. Thus we see that the AK_0 is quite high between $10ms$ and $40ms$ for the different values of the spherical cells permeability. Because the AK_0 is so high at finite permeability, this set of simulations put to question the assumption that the extra-cellular space and the spherical cells can be considered as one physical compartment experiencing Gaussian diffusion at the above diffusion times when the b-values are as high as $2000s/mm^2$.

From the same figure, we also see that when we use a coarser mesh with $h = 0.25\mu m$ (marked by circles), the values of ADC_0 and AK_0 are slightly shifted, with the ADC_0 being lower at the coarser discretization, which is easily explained by the cylinders having more 'jagged' surfaces. However, the behavior of the ADC_0 and AK_0 as a function of

κ^s and diffusion time is consistent with the results from the finer mesh.

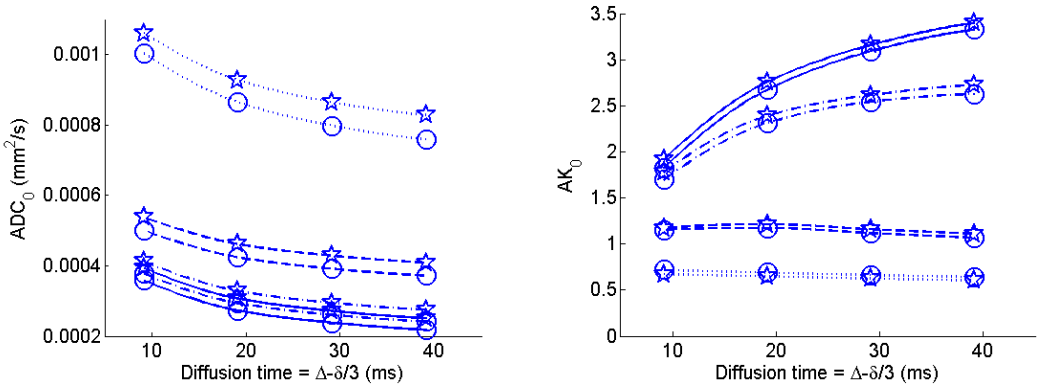

(a) ADC_0 (b) AK_0

FIG. 6 – In the extra-cylindrical compartment comprising of the spherical cells ($v^s = 0.15$) and the extra-cellular space ($v^e = 0.15$) and where the water molecules are stopped from entering the cylindrical cells, the ADC_0 and the AK_0 are computed for the signal arising only from this compartment. Four values of spherical cell permeability : $\kappa^s = 0m/s$ (solid line), $\kappa = 1 \times 10^{-5}m/s$ (dash-dots), $\kappa = 1 \times 10^{-4}m/s$ (dashes), $\kappa = \infty m/s$ (dots), were simulated on two meshes with spatial discretization $h = 0.25\mu m$ (circles) and $h = 0.125\mu m$ (stars).

Details of the numerical method and other simulations can be found in the Preprint listed at the beginning of this section.

5 Formulation of a macroscopic ODE model

Results reported in

1. *A new macroscopic model including membrane exchange for diffusion MRI*, J. Coatléven, H. Haddard, J.-R. Li. Preprint.
2. *Numerical study of a macroscopic ODE model of the diffusion MRI signal*, J.-R. Li ; H. T. Nguyen ; D. V. Nguyen ; H. Haddar ; J. Coatleven ; D. Le Bihan. Preprint.

The Karger model [50] is a system of ordinary differential equations (ODEs) that approximates the dMRI signal and takes into account membrane exchange. It was originally developed for diffusion in zeolites, which are microporous crystalline solids, and the crystal structure can be reasonably thought of as extending infinitely in space. In [87] the relation between the Karger model and the multiple compartment Bloch-Torrey PDE was explored analytically. For dMRI in biological tissue, the Karger model was compared in certain parameter regimes with Monte Carlo simulations [76, 82, 27]. A limitation of the Karger model is that it assumes that the width of the diffusion-encoding pulse is short compared to the diffusion time $\delta \ll \Delta$. In addition, the parameters of the Karger model are the effective diffusion coefficients of the different compartments, and the exchange time between them, but these quantities are described physically, rather than mathematically.

We formulated a system of ODEs governing the time evolution of the integrals of the magnetization in the different physical compartments by an asymptotic analysis on the cell membrane permeability for the multiple compartment Bloch-Torrey PDE. The sum of these integrals at echo time gives the dMRI signal. First the analysis was done for geometries containing compact cells (meaning that the sizes of the cells are small compared to the diffusion distance) and we formulated a new ODE model that does not have a restriction on the width of the gradient pulse. All the parameters of the new ODE model are clearly defined from the geometry and the cell membrane permeability.

In some very recent work (an article describing these results is still under preparation), we generalized the ODE model to geometries containing compact cells as well as long cylindrical cells. We simulated the dMRI signals in complex geometries containing spheres of various sizes and long cylinders of various orientations by solving the multiple compartment Bloch-Torrey PDE in such geometries. Then we computed the dMRI signal predicted by the ODE model and show that it is close to the simulated dMRI signal from the full PDE model. We also simulated the Karger model and showed that when the gradient duration is not short compared to the time between pulses the ODE model offers a much better approximation of the full PDE dMRI signal than the Karger model.

5.1 Heuristic model used by MR physicists

Suppose the concentration of water in each compartment l is u^l, $l = 1, \cdots, P$, then the governing equations for diffusion and exchange between them can be written as :

$$\begin{aligned}
\frac{\partial u^1(\mathbf{r},t)}{\partial t} &= \nabla D^1 \nabla u^1(\mathbf{r},t) - \frac{u^1(\mathbf{r},t)}{w^1} + \sum_{l=2,\cdots,P} \frac{u^l(\mathbf{r},t)}{\tau^{1l}}, \\
&\vdots \\
\frac{\partial u^P(\mathbf{r},t)}{\partial t} &= \nabla D^P \nabla u^P(\mathbf{r},t) - \frac{u^P(\mathbf{r},t)}{w^P} + \sum_{l=1,\cdots,P-1} \frac{u^l(\mathbf{r},t)}{\tau^{Pl}},
\end{aligned} \tag{80}$$

where $\mathbf{r} \in \mathbb{R}^3$, τ^{lm} is the exchange time between the compartment l and m, and D^l is the *effective* diffusion coefficient of compartment l. What is implied by (80) is that all compartments cover all of $\mathbb{R}^3$. The assumption is acceptable to describe diffusion in zeolites, which are microporous crystalline solids, where the crystal structure can be reasonably thought of as extending infinitely in space. For biological cells whose size is not long compared to diffusion distance, this assumption must be examined.

From the mass conservation, if we assume that the water density is the same in all the compartments, $w^1, \cdots, w^P$, must satisfy :

$$\frac{1}{w^m} = \frac{1}{v^m} \sum_{l=1,\, l\neq m}^{P} \frac{v^l}{\tau^{ml}}, \quad m = 1, \cdots, P, \tag{81}$$

where v^l is the volume fraction of compartment l. The system of PDEs in (80) are subject to initial conditions :

$$u^l(\mathbf{r}, 0) = v^l \tilde{\delta}(\mathbf{r}),\ l = 1, \cdots, P, \tag{82}$$

the $\tilde{\delta}(\mathbf{r})$ being the Dirac delta distribution at $\mathbf{r} = 0$. We used the notation $\tilde{\delta}$ to distinguish it from the width of the diffusion-encoding gradient pulse δ.

In the Karger model, a partial signal $S^l(\mathbf{g}, t)$, arising from compartment l, was defined, and under the narrow pulse approximation, assumed to have the following form :

$$S^l(\mathbf{g}, t) \approx \int_{\mathbf{r}\in\mathbb{R}^3} e^{I\delta\mathbf{g}\cdot\mathbf{r}} u^l(\mathbf{r}, t) d\mathbf{r}. \tag{83}$$

We note that the region of integration is $\mathbb{R}^3$. Taking the time derivative of S^l in (83) and using Green's identity, the Karger model can be obtained :

$$\frac{dS^m(\mathbf{g}, t)}{dt} = -\left(D^m \delta^2 \gamma^2 \|\mathbf{g}\|^2 + \frac{1}{v^m} \sum_{l=1,\, l\neq m}^{P} \frac{v^l}{\tau^{ml}} \right) S^1(\mathbf{g}, t) + \sum_{l=1,\, l\neq m}^{P} \frac{1}{\tau^{1l}} S^l(\mathbf{g}, t),\ m = 1, \cdots, P. \tag{84}$$

It is a system of coupled ODEs, subject to the initial conditions :

$$S^l(\mathbf{g}, 0) = v^l,\ l = 1, \cdots, P. \tag{85}$$

In the case where the number of compartments $P = 2, 3$ is small, the analytical solution of (84) can be obtained by finding the eigen-decomposition of a $P \times P$ matrix.

In the original Karger model, the dMRI signal is the sum of the signal from all the compartments at $t = \Delta$:

$$S(\mathbf{g}, \Delta) = \sum_{l=1}^{P} S^l(\mathbf{g}, \Delta).$$

We found that the Karger model can be made somewhat more accurate when we evaluate the signal at $t = \Delta - \delta/3$, thus, we will use

$$S(\mathbf{g}, \Delta - \delta/3) = \sum_{l=1}^{P} S^l(\mathbf{g}, \Delta - \delta/3), \tag{86}$$

when comparing the Karger model with the new ODE model to be described next.

5.2 New ODE model

Even though the Karger model has been used in biological tissue dMRI, there is a question of the exact meaning of (80), given that biological cells are limited in physical size.

We redefined the partial signal $S^l(\mathbf{g}, t)$ as the integral of the solution of the multiple compartments Bloch-Torrey PDE in Ω^l :

$$S^l(\mathbf{g}, t) = \int_{\mathbf{r}\in\Omega^l} M^l(\mathbf{r}, t|, \mathbf{g})\ d\mathbf{r}, l = 1, \cdots, P. \tag{87}$$

We note that in the definition of (87), the range of $\mathbf{r}$ is in Ω^l and not in all of $\mathbb{R}^3$ like in (83). This is a more physically reasonable definition for biological cells and it is mathematically rigorous.

By doing an asymptotic analysis on κ, the permeability coefficient, we obtained a homogenized model for the multiple compartment Bloch-Torrey PDE (12, 13, 14,15, 16, 17). We then showed that the partial signals satisfy a system of coupled ODEs :

$$\frac{dS^m(\mathbf{g},t)}{dt} = -\left(c(t)\gamma^2\mathbf{g}^T\overline{D}^m\mathbf{g} + \frac{1}{v^m}\sum_{l=1,\, l\neq m}^{P}\frac{v^l}{\tau^{ml}}\right)S^m(\mathbf{g},t) + \sum_{l=1,\, l\neq m}^{P}\frac{1}{\tau^{ml}}S^l(\mathbf{g},t),\ m=1,\cdots,P, \tag{88}$$

where we proved that τ^{ml}, the coefficient in row m and column l of the ODE system, is :

$$\frac{1}{\tau^{ml}} = \kappa\frac{\Gamma^{ml}}{V^m}, \tag{89}$$

Γ^{ml} being the surface between Ω^m and Ω^l, and V^m is the volume of Ω^m.

The mathematical derivation of the function $c(t)$ from the full multiple compartment Bloch-Torrey PDE can be found in our preprint. Here we use a more intuitive derivation, by looking at the ODE satisfied by the integral of the solution of the Bloch-Torrey PDE in a *homogeneous* medium. In [52] it was shown for the general gradient time profile $f(s)$, by the use the Laplace transform, the integral of the magnetization satisfies, for any point in time t :

$$S^{hom}(\mathbf{g},t) := \int_{\mathbb{R}^3} m(\mathbf{r},t|\mathbf{g})d\mathbf{r} = e^{-D\gamma^2\|\mathbf{g}\|^2\int_0^t du\left(\int_0^u f(s)ds\right)^2}, \quad t\geq 0.$$

We note that the above equation is valid for any $t \geq 0$, not just at echo time TE. Then we *define* $c(t)$ as :

$$c(t) := \frac{-\frac{\partial S^{hom}(\mathbf{g},t)}{\partial t}}{D\gamma^2\|\mathbf{g}\|^2 S^{hom}(\mathbf{g},t)} = \left(\int_0^t f(s)ds\right)^2, \tag{90}$$

for any profile $f(s)$. For the PGSE sequence,

$$c(t) = \begin{cases} t^2, & 0\leq t\leq\delta, \\ \delta^2, & \delta < t < \Delta, \\ (t-\Delta-\delta)^2, & \Delta < t \leq \Delta+\delta. \end{cases} \tag{91}$$

In the narrow pulse regime, $\delta \leq \Delta$, we can see that (91) becomes one interval and on that interval we obtain the coefficient δ^2 as in the Karger model (84).

In the Karger paper, the precise definitions of the effective diffusion coefficients were not discussed. In our preprint, we showed that if the size of Ω^m is small compared to the diffusion distance, then its effective diffusion tensor is 0 :

$$\overline{D}^m = 0. \tag{92}$$

For the extra-cellular space, we showed how to compute $\overline{D}^m$ if we assume the periodic extension of $C = [-L/2, L/2]^3$ to all of $\mathbb{R}^d$. It is :

$$\overline{D}^m_{j,k} = \frac{1}{v^m}\int_{\Omega^m} D(\mathbf{r})\nabla M_j(\mathbf{r})\cdot\mathbf{e}_k\, d\mathbf{r}, \quad j,k = 1,\cdots,d, \tag{93}$$

where $\mathbf{e}_k$ is the unit vector in the k^{th} direction, and we have to solve d steady-state Laplace equations over C for the unknown function M_j :

$$\nabla \cdot (D(\mathbf{r})\nabla M_j(\mathbf{r})) = 0, \quad \mathbf{r} \in \Omega^m, \tag{94}$$

subject to *impermeable* boundary condition on $\partial\Omega^m$:

$$\nabla M_j(\mathbf{a}) \cdot \mathbf{n}(\mathbf{a}) = 0, \quad \mathbf{a} \in \partial\Omega^m, \tag{95}$$

and *periodic* boundary conditions on ∂C :

$$M_j(\mathbf{r})|_{r_k=-L/2} = M_j(\mathbf{r})|_{r_k=L/2} - w_{j,k}L, \; k = 1, \cdots, d, \tag{96}$$

$$\frac{\partial}{\partial r_k} M_j(\mathbf{r})\bigg|_{r_k=-L/2} = \frac{\partial}{\partial r_k} M_j(\mathbf{r})\bigg|_{r_k=L/2}, \; k = 1, \cdots, d, \tag{97}$$

where $w_{j,k} = 1$ if $k = j$, and $w_{j,k} = 0$ otherwise. We note that if the extra-cellular space Ω^m is not a periodically extension of C, then the definition of $\overline{D}^m$ would change, but the form of the ODE system would not change.

In some recent work, for which a preprint is still under preparation, we generalized the ODE model to allow for long cylindrical cells. If Ω^m is a long cylinder, then we set its effective diffusion tensor to :

$$\overline{D}^m = \mathbf{q}^T D^0 \mathbf{q}, \tag{98}$$

where $\mathbf{q}$ is the normalized ($\|\mathbf{q}\| = 1$) vector parallel to the axis of the cylinder. The derivation of this is not difficult.

Finally, we note that if there is no exchange ($\kappa = 0$) between any of the compartments the dMRI signal is

$$S^{NOEX}(b) = \sum_{m=1}^{P} v^m \exp\left(-\frac{\mathbf{g}^T \overline{D}^m \mathbf{g}}{\|\mathbf{g}\|^2} b\right). \tag{99}$$

If the exchange between the compartments ($\kappa = \infty$) are infinitely fast, then the dMRI signal is :

$$S^{NOEX}(b) = \exp\left(-\left(\sum_{m=1}^{P} v^m \frac{\mathbf{g}^T \overline{D}^m \mathbf{g}}{\|\mathbf{g}\|^2}\right) b\right). \tag{100}$$

The Karger model and the new ODE model are formulated to explain the intermediate exchange regime that falls between the two extremes in (99) and (100).

We note that the expressions in (89,92) have been used in previous works (for example, in [27]) for the Karger model. The derivation of our ODE model contains the mathematical justification for these choices. In addition, it is important to have the rigorous mathematical definition of $\overline{D}^m$ in the extra-cellular space shown in (93). Otherwise, it would be too easy to mask the difference between the full PDE dMRI signal and the ODE model approximation by fitting different $\overline{D}^m$ for different pulse sequences. In the following, we compute $\overline{D}^m$ by solving the steady-state problems in (93) for a given geometry, and we will use the same value for all pulse sequences on that geometry.

We end with a numerical example. We solved the Bloch-Torrey PDE in a geometry of 5 layers of cylindrical cells and 4 layers of spherical cells all embedded in the extra-cellular space, see Fig 7(a). The five layers of cylindrical cells contain parallel cylinders that are oriented 0, 26.5, 45, 63.5 and 90 degrees, respectively, from the x-axis (cylinder radius 0.8μm). The 4 layers of spherical cells (sphere radius 1.1μm) are inserted between the 5 layers of cylindrical cells, The cellular permeability for both cylinders and spheres is set to $\kappa = 10^{-5} m/s$. The computed effective extra-cellular diffusion tensor is :

$$\mathbf{D}^e = \begin{bmatrix} 2.29 & 0.00 & 0.11 \\ 0.00 & 2.05 & 0.00 \\ 0.11 & 0.00 & 2.29 \end{bmatrix} \times 10^{-3} mm^2/s.$$

We computed the new ODE model signal and the Karger model signal and compared them to the full PDE signal, for the PGSE sequence $\delta = \Delta = 40ms$. We see in Fig 7(b) that the ODE and the PDE signals are almost indistinguishable. The Karger model, on the other hand, is far from the PDE signal, because the narrow pulse assumption does not hold, since $\delta = \Delta = 40ms$. Also we see that the PDE signal falls between the no exchange and the fast exchange limits.

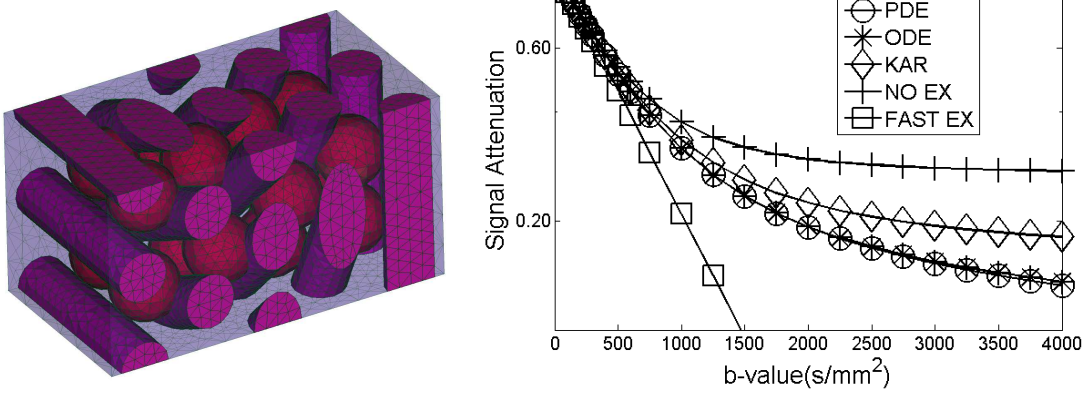

(a) Variably-oriented cylindrical cells and spherical cells.

(b) DMRI signal attenuation

FIG. 7 – Left : mesh of the geometry in the computational domain C. The cell membrane permeability is $\kappa = 10^{-5} m/s$. Right : the simulated dMRI signal from the Bloch-Torrey PDE is labeled 'PDE', the signal from the new ODE model is labeled 'ODE', the signal from the Karger model is labeled 'KAR', the theoretical signal without exchange is labeled 'NO EX', and theoretical signal with fast exchange 'FAST'. The gradient direction is $g = (1, 0, 0)$, the pulse sequence is PGSE, with pulse width $\delta = 40$ms and the delay between two pulses is $\Delta = 40$ms.

6 Current PhD supervision

Results reported in

1. *A finite elements method to solve the Bloch-Torrey equation applied to diffusion magnetic resonance imaging*,
   D. V. Nguyen, J.-R. Li, D. Grebenkov. Preprint.

6.1 PDE model : finite elements discretization and mesh generation

I am one of the co-advisors of the PhD student Dang Van Nguyen. He is working on the improved numerical solution of the Bloch-Torrey PDE by coupling a finite elements discretization to the RKC method, so that cell geometries can be better approximated than the Cartesian discretization we have used previously. In this case, mesh generation for complicated cellular geometries must be considered. In addition, he works on the simulation and analysis of diffusion inside neurons, by distinguishing contributions to the dMRI signal from the neuronal bodies compared to that from the axons and the dendrites. He is funded by an ANR grant ("SIMUDMRI", Nov 2010- Jan 2014, ANR Program COSINUS).

6.2 ODE model : inverse problem

I also co-advise the PhD student Hang Tuan Nguyen who is working on the inversion of the new ODE model for the purpose of brain tissue parameters estimation. He is funded by a PhD scholarship STITS Orsay (Oct 2010-Sept 2013).

7 Research plan

7.1 Experimental validation of PDE model in the Aplysia ganglia neuronal network

We propose to validate the microscopic multiple compartment Bloch-Torrey PDE model on a neuronal network where the individual neurons are much larger than the neurons in mammals. This animal model is the Aplysia. Performing diffusion experiments on intact isolated ganglia from Aplysia should provide insights to mammalian neuronal networks. The advantage of using the Aplysia ganglia in experimental validation is that it is possible to image the entire ganglia with a spatial resolution that will resolve single cells, because the Aplysia neurons are large (neuronal body diameter on the order of hundreds of microns) compared to mammalian neurons (neuronal body diameter on the order of tens of microns). Because the Aplysia neurons have a high tolerance to non-ideal conditions and are viable for relatively long times without the need for chemical fixation, they can be imaged ex-vivo while still providing insights to the water diffusion in-vivo.

We will create a mesh of the ganglia neuronal network and solve the Bloch-Torrey PDE under a variety of geometrical configurations, while varying the cell membrane permeability. Imaging of the Aplysia ganglia will be performed by Luisa Ciobanu of Neurospin under different experimental conditions. The simulation and the imaging will occur concurrently. Because the Aplysia neurons are large and can be resolved individually on the images, it provides of a way of verifying the estimated cell sizes from the PDE model with the true cell sizes obtained by counting pixels on the images.

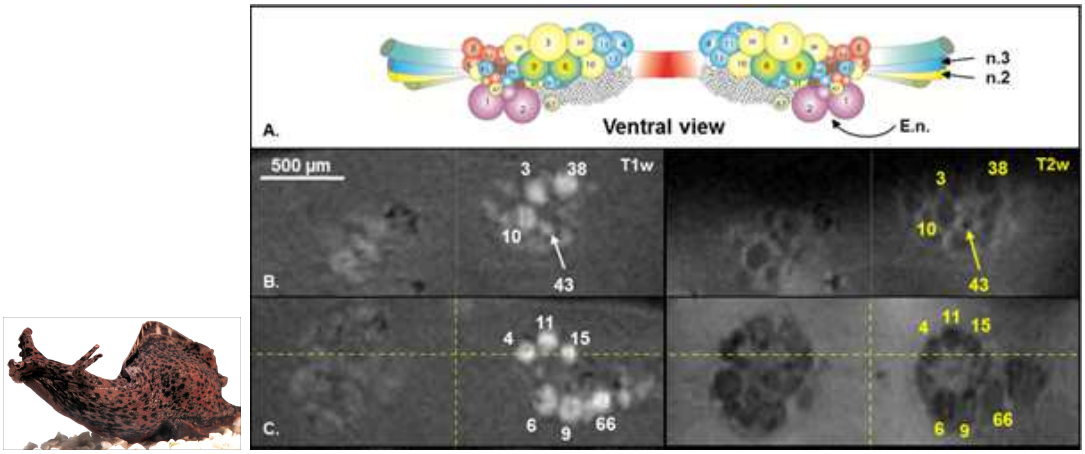

FIG. 8 – Left : Aplysia Californica. Right. A. Schematic of the ventral side of the buccal ganglia. B, C. MR images obtained at 17.2 T (25 μm isotropic resolution). Left column : T1 weighted images obtained using Mn2+ as a contrast agent. The hyperintense regions are cells containing Mn2+. Right column : T2w images. The cells bodies appear hypointense. As indicated by the numbers on the figure, specific neurons have been identified on both T1 and T2 weighted images. Provided by Luisa Ciobanu.

7.2 Inclusion of blood flow in brain micro-vessels in PDE model

In Sept 2013, I will begin a research project "Computational Imaging of the Aging Cerebral Microvasculature", to be funded by the ANR in the Program "US-French Collaboration", Sept 2013- Sept 2016. The goal of the full project is to extract intrinsic micro-vascular parameters in the normal aging brain using MRI and quantify the micro-circulation in the brain which would enable new research in the future examining the variation of the metabolic support of brain neurons and glial cells in aging or disease.

My part in the project focuses on modeling the physics underlying the MRI signal arising from the blood circulation in the micro-vessels in the brain gray matter by PDEs and formulating a reduced model of the MRI signal so that some bio-physical quantities such as the "tortuosity" of the micro-vessels can be robustly obtained from the experimentally obtained MRI signals. The full PDE and the reduce models will both be validated against experimental data in the rat brain to be obtained by the MR physicists at Neurospin. The ANR funding includes the financial support for a PhD student, still to be hired, to be advised jointly by me and Luisa Ciobanu of Neurospin.

FIG. 9 – Image of micro-vessels in the brain. The vessels are small and can be considered "randomly" oriented. Source : *High-Resolution In-Vivo Analysis of Normal Brain Response to Cranial Irradiation*. Burrell K, Hill R, Zadeh G (2012). PLOS ONE. *DOI :10.1371/journal.pone.0038366*

7.3 Macroscopic ODE model at shorter diffusion times

The macroscopic ODE model described previously works well at long diffusion times, or equivalently, when the average cell size is small. We would like to use higher order asymptotics than was done for the current ODE model to allow a better approximation at shorter diffusion times or in the presence of larger cells.

Quatrième partie

Solving the wave equation in complex domains

Sommaire

8 Time integration for complex geometry on embedded Cartesian mesh

Results reported in

1. *High order marching schemes for the wave equation in complex geometry*, J.-R. Li, L. Greengard, Journal of Computational Physics, Volume 198-1, 20 July 2004.
2. *Strongly consistent marching schemes for the wave equation* J.-R. Li, L. Greengard, Journal of Computational Physics, Volume 188-1, 10 June 2003.

Many problems in electromagnetics, optics, and acoustics require the solution of the time-dependent wave equation in complex geometry. We are particularly interested in designing numerical marching schemes that are applicable on Cartesian grids with embedded boundaries as discussed, for example, in [2, 1]. These have a number of advantages over body fitted grids in terms of efficiency, memory consumption, automation, mesh refinement, and convergence analysis. In complicated domains, however, small cells are created wherever the irregular boundary intersects the Cartesian grid. Classical stability analysis [89, 100] suggests that the size of the time step is dependent on the size of the smallest cell in the spatial discretization, rendering such schemes impractical unless some additional techniques are introduced to overcome this restriction. More precisely, we would like to allow time steps on the order of the size of the uniform cells in the grid away from the domain boundary.

Existing approaches to this "small cell" problem include cell merging (see, e.g. [16, 88]), large time step generalizations of Godunov's method [63], and the rotated grid h-box method [7]. In cell merging, one removes small cells near the boundary, which tends to result in a loss of accuracy there. In the generalized Godunov and h-box methods, one keeps the small cells, enlarging the numerical domain of dependence near the small cells in some way. These schemes have not been carried out to high order accuracy. Recent work on Maxwell's equations [25] has demonstrated the feasibility of obtaining second order accuracy using ideas that are somewhat related to those discussed here. Even more closely related is the second order accurate method for the scalar wave equation found in [53]. Nevertheless, for large scale wave propagation problems, high precision is critical to avoid numerical dispersion errors. Hence, there is room for significant improvement in the performance of numerical methods in terms of the order of accuracy.

The schemes we propose follow the work of [3, 65], which introduced a new approach to marching in time that appears to be remarkably insensitive to the presence of small cells. These are three time level schemes, based on an exact evolution formula for wave propagation.

It was shown in [3] that if $u(\mathbf{x}, t)$ is a solution to the homogeneous wave equation

$$\frac{\partial^2 u}{\partial t^2} = \nabla^2 u \tag{101}$$

in $\mathbb{R}^d$, then there exists a kernel $G_d(r, \tau)$ such that

$$u(\mathbf{x}, t+\tau) = 2u(\mathbf{x}, t) - u(\mathbf{x}, t-\tau) + \int_{B_\tau(\mathbf{x})} G_d(|\mathbf{x}-\boldsymbol{\xi}|, \tau)\, \nabla^2 u(\boldsymbol{\xi}, t)\, d\boldsymbol{\xi}, \tag{102}$$

where $B_\tau(\mathbf{x}) = \{\boldsymbol{\xi},\ |\boldsymbol{\xi} - \mathbf{x}| \leq \tau\}$ denotes the closed ball in $\mathbb{R}^d$ of radius τ centered at $\mathbf{x}$. Moreover,

$$G_1(r,\tau) = \tau - r, \tag{103}$$

$$G_2(r,\tau) = \frac{\ln(\tau + \sqrt{\tau^2 - r^2}) - \ln r}{\pi}, \tag{104}$$

$$G_3(r,\tau) = \frac{1}{2\pi r}. \tag{105}$$

We will use the exact formula (102) to construct a class of explicit three time level schemes to solve (101). In particular we modify (102) to solve (101) in a bounded domain D subject to either Dirichlet conditions

$$u(\mathbf{x},t) = g(\mathbf{x},t) \tag{106}$$

or Neumann conditions

$$\frac{\partial u}{\partial \nu} = h(\mathbf{x},t) \tag{107}$$

on the boundary ∂D, where ν is the unit outward normal. We begin by restricting the region of integration in the formula (102) to define $\tilde{u}(\mathbf{x}, t+\tau)$:

$$\tilde{u}(\mathbf{x},t+\tau) := 2u(\mathbf{x},t) - u(\mathbf{x},t-\tau) + \int_{B_\tau(\mathbf{x}) \bigcap \mathcal{D}} G_d(|\mathbf{x} - \boldsymbol{\xi}|, \tau)\, \nabla^2 u(\boldsymbol{\xi}, t)\, d\boldsymbol{\xi}. \tag{108}$$

It is easy to verify that $\tilde{u}$ satisfies the wave equation for $\tau > 0$. As a result, the function S given by

$$S(\mathbf{x},t+\tau) := u(\mathbf{x},t+\tau) - \tilde{u}(\mathbf{x},t+\tau), \qquad \mathbf{x} \in D$$

also satisfies the wave equation and takes on zero initial data. Suppose now that one wants to impose the boundary condition given by (106). Then we must have

$$S(\mathbf{x},t+\tau) = g(\mathbf{x},t+\tau) - \tilde{u}(\mathbf{x},t+\tau), \qquad \mathbf{x} \in \partial D. \tag{109}$$

Similarly, if the boundary condition (107) is to be satisfied, we must have

$$\frac{\partial S}{\partial \nu}(\mathbf{x},t+\tau) = h(\mathbf{x},t+\tau) - \frac{\partial \tilde{u}}{\partial \nu}(\mathbf{x},t+\tau), \qquad \mathbf{x} \in \partial D. \tag{110}$$

In either case, the wave equation for S can be solved using hyperbolic potential theory [33]. For short times τ, this involves a *local boundary integral equation* for which the cost is negligible.

With the boundary conditions given by (106), we represent the solution as a double-layer potential :

$$S(\mathbf{x},t+\tau) = D[\mu](\mathbf{x},\tau) := \int_0^\tau \int_{\boldsymbol{\xi}(\gamma) \in \partial D} \frac{\partial}{\partial \nu(\gamma)} G(\|\mathbf{x} - \boldsymbol{\xi}(\gamma)\|, \tau - \tau')\mu(\gamma,\tau') d\gamma\, d\tau', \tag{111}$$

for $\mathbf{x} \in D$, where $G(r,\tau)$ is the free-space Green's function

$$G(r,\tau) = \begin{cases} 0, & \text{if } r > \tau, \\ 1/\sqrt{\tau^2 - r^2} & \text{if } r < \tau, \end{cases}$$

γ is some parametrization of ∂D, $\nu(\gamma)$ is the unit outward normal at $\boldsymbol{\xi}(\gamma)$, and $\mu(\gamma,\tau')$ is the unknown double-layer density. Taking the limit as $\mathbf{x}$ approaches a point $\boldsymbol{\xi}(\gamma')$ on the boundary, a standard computation [33] yields the relation

$$S(\boldsymbol{\xi}(\gamma'),t+\tau) = -\frac{1}{2}\mu(\gamma',\tau) + \int_0^\tau \int_{\boldsymbol{\xi}(\gamma)\in\partial D} \frac{\partial}{\partial\nu(\gamma)} G(\|\boldsymbol{\xi}(\gamma')-\boldsymbol{\xi}(\gamma)\|,\tau-\tau')\mu(\gamma,\tau')d\gamma\, d\tau' . \tag{112}$$

Thus, the density μ is obtained by solving the following integral equation on the boundary :

$$-\frac{1}{2}\mu(\gamma',\tau) + D_0[\mu](\gamma',\tau) = g(\boldsymbol{\xi}(\gamma'),t+\tau) - \tilde{u}(\boldsymbol{\xi}(\gamma'),t+\tau), \tag{113}$$

where the compact boundary integral operator is

$$D_0[\mu](\gamma',\tau) := \int_0^\tau \int_{\boldsymbol{\xi}(\gamma)\in\partial D} \frac{\partial}{\partial\nu(\gamma)} G(\|\boldsymbol{\xi}(\gamma')-\boldsymbol{\xi}(\gamma)\|,\tau-\tau')\mu(\gamma,\tau')d\gamma\, d\tau' . \tag{114}$$

If the boundary conditions are given by (107), we represent the solution in the form of a single-layer potential :

$$S(\mathbf{x},t+\tau) = S[\sigma](\mathbf{x},\tau) := \int_0^\tau \int_{\boldsymbol{\xi}(\gamma)\in\partial D} G(\|\mathbf{x}-\boldsymbol{\xi}(\gamma)\|,\tau-\tau')\sigma(\gamma,\tau')d\gamma\, d\tau' , \tag{115}$$

for $\mathbf{x}\in D$, where $\sigma(\gamma,\tau')$ is an unknown single-layer density. Taking the appropriate limits, the density σ must solve the following integral equation on the boundary :

$$\frac{1}{2}\sigma(\gamma',\tau) + K_0[\sigma](\gamma',\tau) = h(\boldsymbol{\xi}(\gamma'),t+\tau) - \frac{\partial\tilde{u}}{\partial\nu}(\boldsymbol{\xi}(\gamma'),t+\tau), \tag{116}$$

where the compact boundary integral operator is

$$K_0[\sigma](\gamma',\tau) := \int_0^\tau \int_{\boldsymbol{\xi}(\gamma)\in\partial D} \frac{\partial}{\partial\nu(\gamma')} G(\|\boldsymbol{\xi}(\gamma')-\boldsymbol{\xi}(\gamma)\|,\tau-\tau')\sigma(\gamma,\tau')d\gamma\, d\tau' .$$

Our numerical approach to solving the wave equation (101) in the presence of a boundary is straightforward. At every time step, we discretize (108), march $\tilde{u}$ forward in time, and add the boundary correction $S(\mathbf{x},t+\tau)$, and we showed experimentally that high order schemes in complex geometry are feasible in two space dimensions.

The details can be found in the paper listed at the beginning of this section.

9 Artificial boundary conditions for periodic waveguides containing a local perturbation

Results reported in

1. *Exact boundary conditions for periodic waveguides containing a local perturbation*, P.Joly, J.-R. Li, S.Fliss, Commun. Comput. Phys., 1 (2006), pp. 945-973.

Periodic media play a major role in applications, in particular in optics for micro and nano-technology. From the point of view of applications, one of the main interesting

features is the possibility offered by such media of selecting ranges of frequencies for which waves can or cannot propagate. Mathematically, this property is linked to the gap structure of the spectrum of the underlying differential operator appearing in the model.

There is a need for efficient numerical methods for computing the propagation of waves inside such structures. In real applications, the media are not perfectly periodic but differ from periodic media only in bounded regions (which are small with respect to the total size of the propagation domain). In this case, a natural idea is to reduce the pure numerical computations to these regions and to try to take advantage of the periodic structure of the problem outside : this is particularly of interest when the periodic regions contain a large number of periodicity cells.

Here we contribute to the construction of such methods in a particular situation. We are interested in propagation media that are a local perturbation of an infinite (or very large) periodic waveguide, namely an infinite structure which is periodic in one privileged direction (the propagation direction) and bounded in the other transverse variables (one says that one has a closed waveguide, as opposed to open waveguides as considered in [103], for instance). Physically the perturbation may be a defect or simply a junction. We investigate the question of finding artificial (but exact) boundary conditions to reduce the numerical computation to a neighborhood of this perturbation.

In the case of "classical" waveguides, which are invariant in the propagation direction, (in some sense, periodic with any period), the usual approach consists in applying Dirichlet to Neumann conditions [39, 62] : using the separation of variables, the solution in the semi-infinite waveguide can be written as the superposition of guided modes, that are exponentially varying along the waveguide direction. As a consequence, one can write explicitly a diagonal form of the DtN map in an appropriate (orthonormal) basis. An alternative approach has been proposed recently which uses the method of Perfectly Match Layer (see [6] for the application to waveguides), that does not easily extend to periodic waveguides.

We investigated the generalization of the DtN approach to periodic waveguides, which is complicated by the fact that separation of variables can no longer be used. However, the notion of guided modes has a natural extension : the notion of Floquet modes. By revisiting the Floquet-Bloch theory [54], we propose a method for constructing DtN operators by solving local problems on a single periodicity cell. This is closely connected to operator-valued Riccati equations (here, of a stationary nature), a topic that is already present in many problems concerning artificial boundary conditions (see, for instance, [42, 14]). It appears also that our method is similar to the matrix transfer approach developed for ordinary equations with periodic coefficients [73]. However, except in the 1D case ([86, 28]), this theory cannot be applied directly to our problem due to the fact that the Cauchy problem for the Helmholtz equation is ill-posed in higher dimensions.

The model problem that we consider is that of a 2D periodic waveguide, which allows us to consider a scalar model, but the treatment of the 3D case (where the periodicity is in one direction and the domain bounded in the other two directions) would be similar, in principle. We assume that the geometry as well as the material properties of the waveguide are x-periodic except in a bounded region (see Figure 10). The propagation

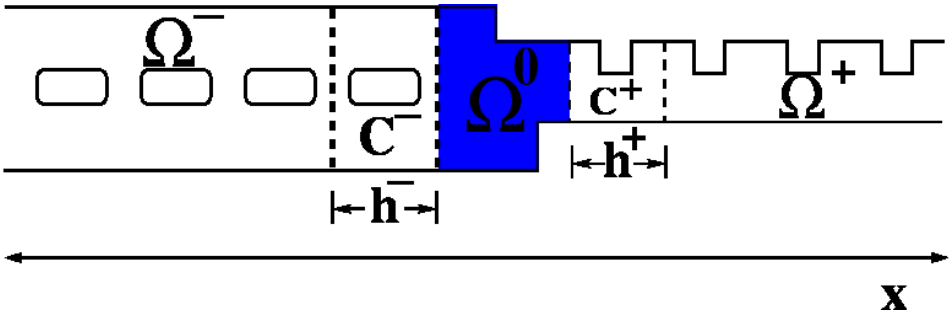

FIG. 10 – Outside the bounded region Ω^0, the geometry as well as the material properties of the waveguide are periodic to the left and to the right. The cells over one period are denoted C^- and C^+, respectively.

model is a simple 2D ($\mathbf{x} = (x, y)$) scalar model :

$$n(\mathbf{x})^2 \, \frac{\partial^2 U(\mathbf{x}, t)}{\partial t^2} - \Delta U(\mathbf{x}, t) = F(\mathbf{x}, t).$$

This model holds in electromagnetism when the 2D model is seen as the cross section of a 3D one, invariant in the z direction. In the case of the transverse electric polarization, U represents the z-component of the electric field and $n(\mathbf{x}) \in L^\infty$ is the index of refraction of the medium. Moreover, we suppose that :

$$0 < n_- = \inf_{\mathbf{x}\in\Omega} n(\mathbf{x}) \leq n_+ = \sup_{\mathbf{x}\in\Omega} n(\mathbf{x}) < +\infty.$$

We assume that the source term $F(\mathbf{x}, t) = f(\mathbf{x}) \; e^{-\imath\omega t}$ is time-harmonic with frequency $\omega > 0$, and look for the time-harmonic solution $U(\mathbf{x}, t) = u(\mathbf{x}) \; e^{-\imath\omega t}$ where u satisfies the Helmholtz equation :

$$-\Delta u(\mathbf{x}) - n(\mathbf{x})^2 \, \omega^2 \, u(\mathbf{x}) = f(\mathbf{x}). \tag{117}$$

The domain of propagation Ω is bounded in the y direction, infinite in the x direction, and periodic outside a bounded region $\Omega^0 = \Omega \cap \{ \, a^- < x < a^+ \}$ that also contains the support of f. The two infinite periodic sub-domains $\Omega^\pm = \Omega \cap \{\pm \, x > \pm \, a^\pm\}$ are of the form :

$$\Omega^\pm = \bigcup_{j=0}^{\infty} \left\{ C^\pm \pm (j h^\pm, 0) \right\},$$

where the unit periodicity cells are

$$C^\pm = \Omega \cap \{ \pm \, a^\pm \leq \pm x \leq \pm \, a^\pm + h^\pm \}.$$

The function $n(\mathbf{x})$ is "x-periodic" as well :

$$n(x, y) = n(x \pm h^\pm, y), \;\; (x, y) \in \Omega^\pm.$$

The boundary condition on $\partial\Omega$ (which we suppose to be piecewise C^1 and Lipschitz continuous) can be Dirichlet (this would be consistent with the perfectly conducting boundary condition in electromagnetism), Neumann, or any combination, but they need to be compatible with the periodicity of equation (117) in Ω^- and Ω^+.

We characterized the restriction of u to Ω^0 as the solution of (117) in Ω^0 that satisfies the boundary conditions on the "Ω^0-part" of $\partial\Omega$, and in addition, satisfies boundary conditions of the form

$$\pm\frac{\partial u}{\partial x} + \Lambda^{\pm} u = 0, \tag{118}$$

on the two "vertical" boundaries $\Gamma^{\pm} = \Omega \cap \{x = a^{\pm}\}$. We characterized the operator $\Lambda^{\pm}$ to construct the transparent boundary conditions in (118). The details are given in the paper listed at the beginning of this section.

Cinquième partie

List of publications

Publications list

Papers, preprints, and other material are available online at :
`http://www.cmap.polytechnique.fr/~jingrebeccali/`

Preprints

1. *A new macroscopic model including membrane exchange for diffusion MRI*,
   J. Coatléven, H. Haddard, J.-R. Li.
2. *A finite elements method to solve the Bloch-Torrey equation applied to diffusion magnetic resonance imaging*,
   D. V. Nguyen, J.-R. Li, D. Grebenkov.
3. *Numerical study of a macroscopic ODE model of the diffusion MRI signal*,
   J.-R. Li, H. T. Nguyen, D. V. Nguyen, H. Haddar, J. Coatleven, D. Le Bihan.

Journal articles and refereed conference proceedings

1. *Numerical simulation of diffusion MRI signals using an adaptive time-stepping method*,
   J.-R. Li, D. Calhoun, C. Poupon, D. Le Bihan. Accepted. Physics in Medicine and Biology, 2013.
2. *Diffusion Microscopist Simulator : A General Monte Carlo Simulation System for Diffusion Magnetic Resonance Imaging*,
   C.-H. Yeh, B. Schmitt, D. Le Bihan, J.-R. Li, C.-P. Lin, C. Poupon. Accepted. PLOS ONE, 2013.
3. *A fast random walk algorithm for computing diffusion-weighted NMR signals in multiscale porous media : a feasibility study for a Menger sponge*,
   D. Grebenkov, H.T. Nguyen, J.-R. Li. Accepted. Microporous & Mesoporous Materials, 2013.
4. *A fast time stepping method for evaluating fractional integrals*,
   J.-R. Li, SIAM Journal on Scientific Computing, Vol 31, 2010. pp. 4696-4714.
5. *Fast and accurate computation of layer heat potentials*,
   J.-R. Li, L.Greengard, SIAM Journal on Scientific Computing, Vol 31, 2009. pp. 3847-3860.
6. *Efficient thermal field computation in phase field models*,
   J.-R. Li, D. Calhoun, L. Brush. Journal of Computational Physics, Volume 228, Issue 24, 20 December 2009, Pages 8945-8957.
7. *Efficient solution of a wave equation with fractional order dissipative terms*,
   H. Haddar, J.-R. Li, D. Matignon. Journal of Computational and Applied Mathematics, Volume 234, Issue 6, 15 July 2010, Pages 2003-2010.
8. *Numerical solution of large-scale Lyapunov equations, Riccati equations, and linear-quadratic optimal control problems*,
   P. Benner, J.-R. Li, T. Penzl, Numerical Linear Algebra with Applications, Volume 15, 2008, Pages 755-777.

9. *On the numerical solution of the heat equation I : fast solvers in free space*,
J.-R. Li, L. Greengard, Journal of Computational Physics, Vol. 226-2, 1 Oct. 2007.

10. *Exact boundary conditions for periodic waveguides containing a local perturbation*,
P.Joly, J.-R. Li, S.Fliss, Commun. Comput. Phys., 1 (2006), pp. 945-973.

11. *Low order approximation of the spherical nonreflecting boundary kernel for the wave equation*,
J.-R. Li, Linear Algebra and its Applications, Special Issue on Order Reduction of Large-Scale Systems, Volume 415, Issues 2-3, June 2006.

12. *Smith-Type methods for balanced truncation of large sparse systems*,
S. Gugercin, J.-R. Li, Dimension Reduction of Large-Scale Systems Proceedings of a Workshop held in Oberwolfach, Germany, October 19-25, 2003. Series : Lecture Notes in Computational Science and Engineering , Vol. 45 Benner, Peter ; Mehrmann, Volker ; Sorensen, Danny C. (Eds.) 2005.

13. *Low rank solution of Lyapunov equations*,
J.-R. Li, J. White, SIAM Review, SIGEST selection, issue 46-4, December 2004.

14. *High order marching schemes for the wave equation in complex geometry*,
J.-R. Li, L. Greengard, Journal of Computational Physics, Volume 198-1, 20 July 2004.

15. *Strongly consistent marching schemes for the wave equation*,
J.-R. Li, L. Greengard, Journal of Computational Physics, Volume 188-1, 10 June 2003.

16. *Low rank solution of Lyapunov equations*,
J.-R. Li, J. White, SIAM Journal on Matrix Analysis and Applications, **24** 2002.

17. *Reduction of large circuit models via low rank approximate Gramians*,
J.-R. Li, J. White, International Journal of Applied Math. and Comp. Sci., **11**, 2001.

18. *Efficient Model Reduction of Interconnect via Approximate System Grammians*,
J.-R. Li, J. White, IEEE/ACM International Conference on Computer-Aided Design, 1999. Digest of Technical Papers. 7-11 Nov. 1999.

19. *An Efficient Lyapunov Equation-Based Approach for Generating Reduced Order Models of Interconnect*,
J.-R. Li, F. Wang, J. White, Design Automation Conference, 1999. Proceedings. 36th, 21-25 June 1999.

Sixième partie

References

Références

[1] M. J. Aftosmis, M. Berger, and J. E. Melton. Robust and efficient cartesian mesh generation using for component-based geometry. *AIAA Journal*, 36(6) :952–960, 1998.

[2] A. S. Almgren, J. B. Bell, P. Colella, and T. Marthaler. A cartesian mesh method for the incompressible euler equations in complex geometries. *SIAM J. Scientific Computing*, 142(1) :1–46, 1997.

[3] Bradley Alpert, Leslie Greengard, and Thomas Hagstrom. An integral evolution formula for the wave equation. *J. Comput. Phys.*, 162(2) :536–543, 2000.

[4] Bradley K. Alpert. Hybrid Gauss-trapezoidal quadrature rules. *SIAM J. Sci. Comput.*, 20(5) :1551–1584 (electronic), 1999.

[5] Yaniv Assaf, Tamar Blumenfeld-Katzir, Yossi Yovel, and Peter J. Basser. Axcaliber : A method for measuring axon diameter distribution from diffusion MRI. *Magn. Reson. Med.*, 59(6) :1347–1354, 2008.

[6] E. Bécache, A.-S. Bonnet-Ben Dhia, and G. Legendre. Perfectly matched layers for the convected Helmholtz equation. *SIAM J. Numer. Anal.*, 42(1) :409–433 (electronic), 2004.

[7] Marsha J. Berger and Randall J. LeVeque. A rotated difference scheme for cartesian grids in complex geometries. In *Proceedings, AIAA 10th Computational Fluid Dynamics Conference*, pages 1–9, Honolulu, Hawaii, 1991. AIAA Paper CP-91-1602.

[8] F. Bloch. Nuclear induction. *Phys. Rev.*, 70(7-8) :460–474, October 1946.

[9] R. J. Braun and B. T. Murray. Adaptive phase-field computations of dendritic crystal growth. *Journal of Crystal Growth*, 174(1-4) :41–53, April 1997.

[10] C. A. Brebbia, J. C. F. Telles, and L. C. Wrobel. *Boundary element techniques.* Springer Verlag, Berlin, 1984.

[11] Paul Callaghan. A simple matrix formalism for spin echo analysis of restricted diffusion under generalized gradient waveforms. *Journal of Magnetic Resonance*, 129(1) :74–84, November 1997.

[12] A. Carpinteri and F. Mainardi, editors. *Fractals and fractional calculus in continuum mechanics*, volume 378 of *CISM Courses and Lectures.* Springer-Verlag, Vienna, 1997. Papers from the CISM Course on Scaling Laws and Fractality in Continuum Mechanics held in Udine, September 23–27, 1996.

[13] Steren Chabert, Nicolas Molko, Yann Cointepas, Patrick Le Roux, and Denis Le Bihan. Diffusion tensor imaging of the human optic nerve using a non-CPMG fast spin echo sequence. *J. Magn. Reson. Imaging*, 22(2) :307–310, 2005.

[14] I. Champagne and J. Henry. Riccati equation for the impedance of waveguides. In *Mathematical and numerical aspects of wave propagation—WAVES 2003*, pages 457–462. Springer, Berlin, 2003.

[15] Anindya Chatterjee. Statistical origins of fractional derivatives in viscoelasticity. *Journal of Sound and Vibration*, 284(3-5) :1239–1245, June 2005.

[16] William J. Coirier and Kenneth G. Powell. An accuracy assessment of Cartesian-mesh approaches for the Euler equations. *J. Comput. Phys.*, 117(1) :121–131, 1995.

[17] M. Costabel. Time-dependent problems with the boundary integral equation. In E. Stein, R. de Borst, and T. J. R. Hughes, editors, *Encyclopedia of Computational Mechanics*, pages 703–721. John Wiley & Sons, 2004.

[18] G. F. Dargush and P. K. Banerjee. Application of the boundary element method to transient heat conduction. *International Journal for Numerical Methods in Engineering*, 1991.

[19] P. J. Davis and P. Rabinowitz. *Methods of numerical integration*. Academic Press, San Diego, 1984.

[20] S. H. Davis. *Theory of Solidification*. Cambridge University Press, Cambridge, England, 2001. Cambridge Monographs on Mechanics.

[21] Lokenath Debnath. Recent applications of fractional calculus to science and engineering. *Int. J. Math. Math. Sci.*, (54) :3413–3442, 2003.

[22] K. Diethelm, N. J. Ford, A. D. Freed, and Yu. Luchko. Algorithms for the fractional calculus : a selection of numerical methods. *Comput. Methods Appl. Mech. Engrg.*, 194(6-8) :743–773, 2005.

[23] Kai Diethelm. An investigation of some nonclassical methods for the numerical approximation of caputo-type fractional derivatives. *Numerical Algorithms*, 47(4) :361–390, April 2008.

[24] Kai Diethelm, Judith M. Ford, Neville J. Ford, and Marc Weilbeer. Pitfalls in fast numerical solvers for fractional differential equations. *Journal of Computational and Applied Mathematics*, 186(2) :482 – 503, 2006.

[25] A. Ditkowski, K. Dridi, and J. S. Hesthaven. Convergent cartesian grid methods for maxwell's equations in complex geometries. *Journal of Computational Physics*, 170(1) :39–80, June 2001.

[26] Eric Dubach. Artificial boundary conditions for diffusion equations : numerical study. *J. Comput. Appl. Math.*, 70(1) :127–144, 1996.

[27] Els Fieremans, Dmitry S. Novikov, Jens H. Jensen, and Joseph A. Helpern. Monte carlo study of a two-compartment exchange model of diffusion. *NMR in Biomedicine*, 23(7) :711–724, 2010.

[28] A. Figotin and V. Gorentsveig. Localized electromagnetic waves in a periodic-layered dielctric medium with a defect. *Phys. Rev. B*, 58(1) :180–188, july 1998.

[29] Zydrunas Gimbutas and Vladimir Rokhlin. A generalized fast multipole method for nonoscillatory kernels. *SIAM Journal of Scientific Computing*, 24(3) :796–817, 2002.

[30] Denis Grebenkov. A fast random walk algorithm for computing the pulsed-gradient spin-echo signal in multiscale porous media. *Journal of Magnetic Resonance*, 208(2) :243 – 255, 2011.

[31] Leslie Greengard and Patrick Lin. Spectral approximation of the free-space heat kernel. *Appl. Comput. Harmon. Anal.*, 9(1) :83–97, 2000.

[32] Leslie Greengard and John Strain. A fast algorithm for the evaluation of heat potentials. *Comm. Pure Appl. Math.*, 43(8) :949–963, 1990.

[33] Ronald B. Guenther and John W. Lee. *Partial differential equations of mathematical physics and integral equations*. Prentice Hall, Inglewood Cliffs, New Jersey, 1988.

[34] Thomas Hagstrom. Radiation boundary conditions for the numerical simulation of waves. In *Acta numerica, 1999*, volume 8 of *Acta Numer.*, pages 47–106. Cambridge Univ. Press, Cambridge, 1999.

[35] E. Hairer, Ch. Lubich, and M. Schlichte. Fast numerical solution of nonlinear Volterra convolution equations. *SIAM J. Sci. Statist. Comput.*, 6(3) :532–541, 1985.

[36] L. Halpern and J. Rauch. Absorbing boundary conditions for diffusion equations. *Numer. Math.*, 71(2) :185–224, 1995.

[37] Houde Han and Zhongyi Huang. A class of artificial boundary conditions for heat equation in unbounded domains. *Comput. Math. Appl.*, 43(6-7) :889–900, 2002.

[38] Houde Han and Zhongyi Huang. Exact and approximating boundary conditions for the parabolic problems on unbounded domains. *Comput. Math. Appl.*, 44(5-6) :655–666, 2002.

[39] I. Harari, I. Patlashenko, and D. Givoli. Dirichlet-to-Neumann maps for unbounded wave guides. *J. Comput. Phys.*, 143(1) :200–223, 1998.

[40] Kevin D. Harkins, Jean-Philippe Galons, Timothy W. Secomb, and Theodore P. Trouard. Assessment of the effects of cellular tissue properties on ADC measurements by numerical simulation of water diffusion. *Magn. Reson. Med.*, 62(6) :1414–1422, 2009.

[41] Th. Hélie and D. Matignon. Diffusive representations for the analysis and simulation of flared acoustic pipes with visco-thermal losses. *Math. Models Methods Appl. Sci.*, 16(4) :503–536, 2006.

[42] J. Henry and A. M. Ramos. Factorization of second-order elliptic boundary value problems by dynamic programming. *Nonlinear Anal.*, 59(5) :629–647, 2004.

[43] Scott N. Hwang, Chih-Liang Chin, Felix W. Wehrli, and David B. Hackney. An image-based finite difference model for simulating restricted diffusion. *Magnetic Resonance in Medicine*, 50(2) :373–382, 2003.

[44] M. T. Ibanez and H. Power. An efficient direct bem numerical scheme for phase change problems using fourier series. *Computer Methods in Applied Mechanics and Engineering*, 2002.

[45] Jens H. Jensen, Joseph A. Helpern, Anita Ramani, Hanzhang Lu, and Kyle Kaczynski. Diffusional kurtosis imaging : The quantification of non-Gaussian water diffusion by means of magnetic resonance imaging. *Magnetic Resonance in Medicine*, 53(6) :1432–1440, 2005.

[46] Sune N. Jespersen, Carsten R. Bjarkam, Jens R. Nyengaard, M. Mallar Chakravarty, Brian Hansen, Thomas Vosegaard, Leif Astergaard, Dmitriy Yablonskiy, Niels Chr. Nielsen, and Peter Vestergaard-Poulsen. Neurite density from magnetic resonance diffusion measurements at ultrahigh field : Comparison with light microscopy and electron microscopy. *NeuroImage*, 49(1) :205–216, January 2010.

[47] Sune N. Jespersen, Christopher D. Kroenke, Leif Ãstergaard, Joseph J.H. Ackerman, and Dmitriy A. Yablonskiy. Modeling dendrite density from magnetic resonance diffusion measurements. *NeuroImage*, 34(4) :1473–1486, February 2007.

[48] T Jochimsen, A Schafer, R Bammer, and M Moseley. Efficient simulation of magnetic resonance imaging with bloch-torrey equations using intra-voxel magnetization gradients. *Journal of Magnetic Resonance*, pages –, January 2006.

[49] Sharad Kapur and Vladimir Rokhlin. High-order corrected trapezoidal quadrature rules for singular functions. *SIAM J. Numer. Anal.*, 34(4) :1331–1356, 1997.

[50] J. Karger, H. Pfeifer, and W. Heinik. Principles and application of self-diffusion measurements by nuclear magnetic resonance. *Advances in magnetic resonance*, 12 :1–89, 1988.

[51] Alain Karma and Wouter-Jan Rappel. Phase-field method for computationally efficient modeling of solidification with arbitrary interface kinetics. *Phys. Rev. E*, 53(4) :R3017–R3020, Apr 1996.

[52] V Kenkre. Simple solutions of the Torrey-Bloch equations in the NMR study of molecular diffusion. *Journal of Magnetic Resonance*, 128(1) :62–69, September 1997.

[53] Heinz-Otto Kreiss, N. Anders Petersson, and Jacob Yström. Difference approximations for the second order wave equation. *SIAM J. Numer. Anal.*, 40(5) :1940–1967 (electronic), 2002.

[54] P. Kuchment. *Floquet theory for partial differential equations*, volume 60 of *Operator Theory : Advances and Applications*. Birkhäuser Verlag, Basel, 1993.

[55] W. Kurz. *Fundamentals of Solidification*. Trans Tech, Aedermannsdorf, Switzerland, 1992.

[56] J. C. LaCombe, M. B. Koss, D. C. Corrigan, A. O. Lupulescu, L. A. Tennenhouse, and M.E. Glicksman. Implications of the interface shape on steady-state dendritic crystal growth. *J. of Crystal Growth*, 206 :331–344, 1999.

[57] J. S. Langer. Instabilities and pattern formation in crystal growth. *Rev. Mod. Phys.*, 52 :1–28, 1980.

[58] Mariana Lazar. Mapping brain anatomical connectivity using white matter tractography. *NMR Biomed.*, 23(7) :821–835, 2010.

[59] D Le Bihan, E Breton, D Lallemand, P Grenier, E Cabanis, and M Laval-Jeantet. MR imaging of intravoxel incoherent motions : application to diffusion and perfusion in neurologic disorders. *Radiology*, 161(2) :401–407, 1986.

[60] Denis Le Bihan and Heidi Johansen-Berg. Diffusion MRI at 25 : Exploring brain tissue structure and function. *NeuroImage*, 61(2) :324–341, June 2012.

[61] Denis LeBihan, Shin-ichi Urayama, Toshihiko Aso, Takashi Hanakawa, and Hidenao Fukuyama. Direct and fast detection of neuronal activation in the human brain with diffusion mri. *PNAS*, 103(21) :8263–8268, 2006.

[62] M. Lenoir and A. Tounsi. The localized finite element method and its application to the two-dimensional sea-keeping problem. *SIAM J. Numer. Anal.*, 25(4) :729–752, 1988.

[63] Randall J. LeVeque. A large time step generalization of Godunov's method for systems of conservation laws. *SIAM J. Numer. Anal.*, 22(6) :1051–1073, 1985.

[64] Jing-Rebecca Li. A fast time stepping method for evaluating fractional integrals. *SIAM J. Sci. Comput.*, 31(6) :4696–4714, January 2010.

[65] Jing-Rebecca Li and Leslie Greengard. Strongly consistent marching schemes for the wave equation. *Journal of Computational Physics*, 188(1) :194–208, June 2003.

[66] Maria Lopez-Fernandez, Christian Lubich, and Achim Schadle. Adaptive, fast, and oblivious convolution in evolution equations with memory. *SIAM Journal on Scientific Computing*, 30(2) :1015–1037, 2008.

[67] Jian-Fei Lu and Andrzej Hanyga. Wave field simulation for heterogeneous porous media with singular memory drag force. *Journal of Computational Physics*, 208(2) :651–674, September 2005.

[68] Ch. Lubich. Discretized fractional calculus. *SIAM J. Math. Anal.*, 17(3) :704–719, 1986.

[69] Ch. Lubich and A. Ostermann. Runge-Kutta methods for parabolic equations and convolution quadrature. *Math. Comp.*, 60(201) :105–131, 1993.

[70] Ch. Lubich and R. Schneider. Time discretization of parabolic boundary integral equations. *Numer. Math.*, 63(4) :455–481, 1992.

[71] Christian Lubich and Achim Schädle. Fast convolution for nonreflecting boundary conditions. *SIAM J. Sci. Comput.*, 24(1) :161–182 (electronic), 2002.

[72] J. Ma, V. Rokhlin, and S. Wandzura. Generalized Gaussian quadrature rules for systems of arbitrary functions. *SIAM J. Numer. Anal.*, 33(3) :971–996, 1996.

[73] W. Magnus and S. Winkler. *Hill's equation.* Interscience Tracts in Pure and Applied Mathematics, No. 20. Interscience Publishers John Wiley & Sons New York-London-Sydney, 1966.

[74] Stephan E. Maier, Yanping Sun, and Robert V. Mulkern. Diffusion imaging of brain tumors. *NMR Biomed.*, 23(7) :849–864, 2010.

[75] Denis Matignon. Stability properties for generalized fractional differential systems. In *Systèmes différentiels fractionnaires (Paris, 1998)*, volume 5 of *ESAIM Proc.*, pages 145–158. Soc. Math. Appl. Indust., Paris, 1998.

[76] Christian Meier, Wolfgang Dreher, and Dieter Leibfritz. Diffusion in compartmental systems. i. a comparison of an analytical model with simulations. *Magnetic Resonance in Medicine*, 50(3) :500–509, 2003.

[77] Gerard Montseny. Diffusive representation of pseudo-differential time-operators. *ESAIM : Proceedings*, 5 :159–175, 1998.

[78] Gérard Montseny, Jacques Audounet, and Denis Matignon. Diffusive representation for pseudo-differentially damped nonlinear systems. In *Nonlinear control in the year 2000, Vol. 2 (Paris)*, volume 259 of *Lecture Notes in Control and Inform. Sci.*, pages 163–182. Springer, London, 2001.

[79] ME Moseley, J Kucharczyk, J Mintorovitch, Y Cohen, J Kurhanewicz, N Derugin, H Asgari, and D Norman. Diffusion-weighted MR imaging of acute stroke : correlation with T2- weighted and magnetic susceptibility-enhanced MR imaging in cats. *AJNR Am J Neuroradiol*, 11(3) :423–429, 1990.

[80] B. T. Murray, W. J. Boettinger, G. B. McFadden, and A. A. Wheeler. Computation of dendritic solidification using a phase-field model. *ASME Heat Transfer Melting, Solidification Cryst. Growth*, 234 :67, 1993.

[81] B. T. Murray, A. A. Wheeler, and M. E. Glicksman. Simulations of experimentally observed dendritic growth behavior using a phase-field model. *Journal of Crystal Growth*, 154(3-4) :386–400, September 1995.

[82] M. Nilsson, E. Alerstam, R. Wirestam, F. Stahlberg, S. Brockstedt, and J. Latt. Evaluating the accuracy and precision of a two-compartment Karger model using monte carlo simulations. *Journal of Magnetic Resonance*, 206(1) :59 – 67, 2010.

[83] Josef Pfeuffer, Ulrich Flogel, Wolfgang Dreher, and Dieter Leibfritz. Restricted diffusion and exchange of intracellular water : theoretical modelling and diffusion time dependence of 1H NMR measurements on perfused glial cells. *NMR in Biomedicine*, 11(1) :19–31, 1998.

[84] Igor Podlubny. *Fractional differential equations*, volume 198 of *Mathematics in Science and Engineering*. Academic Press Inc., San Diego, CA, 1999. An introduction to fractional derivatives, fractional differential equations, to methods of their solution and some of their applications.

[85] Witold Pogorzelski. *Integral equations and their applications*. Pergamon Press, Oxford, 1966.

[86] C. Potel, Ph. Gatignol, and J.F De Belleval. Energetic criterion for the radiation of floquet waves in infinite anisotropic periodically multilayered media. *Acustica-Acta Acustica*, 87(3) :340–351, 2001.

[87] William S. Price, Alexander V. Barzykin, Kikuko Hayamizu, and M. Tachiya. A model for diffusive transport through a spherical interface probed by pulsed-field gradient NMR. *Biophysical Journal*, 74(5) :2259–2271, May 1998.

[88] J.J. Quirk. An alternative to unstructured grids for computing gas dynamic flows around arbitrarily complex two-dimensional bodies. *Computers and Fluids*, 23(1) :125–42, Jan. 1994.

[89] Robert D. Richtmyer and K. W. Morton. *Difference methods for initial-value problems*. Interscience Publishers John Wiley & Sons, Inc., New York-London-Sydney, 1967.

[90] J. Rosam, P.K. Jimack, and A. Mullis. A fully implicit, fully adaptive time and space discretisation method for phase-field simulation of binary alloy solidification. *Journal of Computational Physics*, 225(2) :1271–1287, August 2007.

[91] Greg Russell, Kevin D Harkins, Timothy W Secomb, Jean-Philippe Galons, and Theodore P Trouard. A finite difference method with periodic boundary conditions for simulations of diffusion-weighted magnetic resonance experiments in tissue. *Physics in Medicine and Biology*, 57(4) :N35, 2012.

[92] Achim Schadle, Maria Lopez-Fernandez, and Christian Lubich. Fast and oblivious convolution quadrature. *SIAM J. Sci. Comput.*, 28(2) :421–438, January 2006.

[93] André Schmidt and Lothar Gaul. On a critique of a numerical scheme for the calculation of fractionally damped dynamical systems. *Mechanics Research Communications*, 33(1) :99–107, 2006.

[94] Pabitra N. Sen and Peter J. Basser. A model for diffusion in white matter in the brain. *Biophys J*, 89(5) :2927–2938, November 2005.

[95] B. P. Sommeijer, L. F. Shampine, and J. G. Verwer. RKC : An explicit solver for parabolic PDEs. *Journal of Computational and Applied Mathematics*, 88(2) :315–326, March 1998.

[96] Olof J. Staffans. Well-posedness and stabilizability of a viscoelastic equation in energy space. *Transactions of the American Mathematical Society*, 345(2) :527–575, 1994.

[97] E. O. Stejskal and J. E. Tanner. Spin diffusion measurements : Spin echoes in the presence of a time-dependent field gradient. *The Journal of Chemical Physics*, 42(1) :288–292, 1965.

[98] S. D. Stoller, W. Happer, and F. J. Dyson. Transverse spin relaxation in inhomogeneous magnetic fields. *Phys. Rev. A*, 44(11) :7459–7477, December 1991.

[99] John Strain. Fast adaptive methods for the free-space heat equation. *SIAM J. Sci. Comput.*, 15(1) :185–206, 1994.

[100] John C. Strikwerda. *Finite difference schemes and partial differential equations*. Wadsworth & Brooks/Cole Advanced Books & Software, Pacific Grove, CA, 1989.

[101] Takeshi Sugahara, Yukunori Korogi, Masato Kochi, Ichiro Ikushima, Yoshinori Shigematu, Toshinori Hirai, Tomoko Okuda, Luxia Liang, Yulin Ge, Yasuyuki Komohara, Yukitaka Ushio, and Mutsumasa Takahashi. Usefulness of diffusion-weighted MRI with echo-planar technique in the evaluation of cellularity in gliomas. *J. Magn. Reson. Imaging*, 9(1) :53–60, 1999.

[102] Alexander L Sukstanskii and Dmitriy A Yablonskiy. Effects of restricted diffusion on MR signal formation. *Journal of Magnetic Resonance*, 157(1) :92–105, July 2002.

[103] J. Tausch and J. Butler. Floquet multipliers of periodic waveguides via Dirichlet-to-Neumann maps. *J. Comput. Phys.*, 159(1) :90–102, 2000.

[104] Johannes Tausch. A fast method for solving the heat equation by layer potentials. *Journal of Computational Physics*, 224(2) :956–969, June 2007.

[105] R. Tonhardt and G. Amberg. Phase-field simulation of dendritic growth in a shear flow. *J. of Crystal Growth*, 194 :406–425, 1998.

[106] HC Torrey. Bloch equations with diffusion terms. *Physical Review Online Archive (Prola)*, 104(3) :563–565, 1956.

[107] C. Trinks and P. Ruge. Treatment of dynamic systems with fractional derivatives without evaluating memory-integrals. *Comput. Mech.*, 29(6) :471–476, 2002.

[108] Yoshito Tsushima, Ayako Takahashi-Taketomi, and Keigo Endo. Magnetic resonance (MR) differential diagnosis of breast tumors using apparent diffusion coefficient (adc) on 1.5-t. *J. Magn. Reson. Imaging*, 30(2) :249–255, 2009.

[109] S. L. Wang and R. F. Sekerka. Algorithms for Phase Field Computation of the Dendritic Operating State at Large Supercoolings. *J. of Comp. Phys*, 127 :110–117, 1996.

[110] S. Warach, D. Chien, W. Li, M. Ronthal, and R. R. Edelman. Fast magnetic resonance diffusion-weighted imaging of acute human stroke. *Neurology*, 42(9) :1717–, 1992.

[111] A.A. Wheeler, B.T. Murray, and R.J. Schaefer. Computation of dendrites using a phase field model. *Physica D : Nonlinear Phenomena*, 66(1-2) :243–262, June 1993.

[112] J Xu, MD Does, and JC Gore. Numerical study of water diffusion in biological tissues using an improved finite difference method. *Physics in medicine and biology*, 52(7), April 2007.

[113] Lexing Ying, George Biros, and Denis Zorin. A kernel-independent adaptive fast mulitpole method in two and three dimensions. *Journal of Computational Physics*, 196(2) :591–626, 2004.

[114] Lixia Yuan and Om P. Agrawal. A numerical scheme for dynamic systems containing fractional derivatives. *J. Vib. Acoust.*, 124(2) :321–324, April 2002.